Article

Cancer Cell

Druggable growth dependencies and tumor evolution analysis in patient-derived organoids of neuroendocrine neoplasms from multiple body sites

Graphical abstract

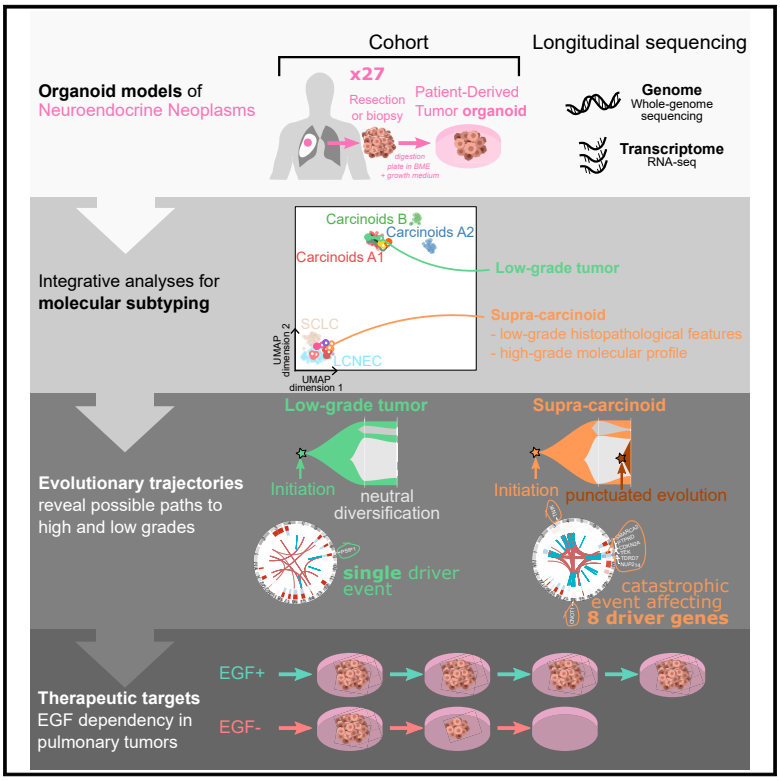

Highlights

- PDTOs of NETs and LCNEC from multiple sites were established
- PDTOs recapitulate intra-tumoral heterogeneity and evolution of parental tumors
- Drug assays reveal therapeutic vulnerabilities and biomarkers
- Pulmonary NET PDTOs are dependent on EGF

Authors

Talya L. Dayton, Nicolas Alcala, Laura Moonen, ..., Matthieu Foll, Lynnette Fernández-Cuesta, Hans Clevers

Correspondence

talya.dayton@embl.es (T.L.D.), fernandezcuestal@iarc.who.int (L.F.-C.), h.clevers@hubrecht.eu (H.C.)

In brief

Dayton et al. established patient-derived tumor organoids (PDTOs) from neuroendocrine neoplasms including low-grade pulmonary neuroendocrine tumors. Multi-omic molecular analyses show that PDTOs retain parental tumor intra-tumoral heterogeneity. Phenotypic growth analyses reveal EGF dependency of a subset of pulmonary neuroendocrine tumors, indicating a therapeutic vulnerability in these tumors.

Dayton et al., 2023, Cancer Cell *41*, 2083–2099
December 11, 2023
https://doi.org/10.1016/j.ccell.2023.11.007

CellPress

Cancer Cell

CellPress
OPEN ACCESS

Article

Druggable growth dependencies and tumor evolution analysis in patient-derived organoids of neuroendocrine neoplasms from multiple body sites

Talya L. Dayton,[1,2,17,19,*] Nicolas Alcala,[3,17] Laura Moonen,[4] Lisanne den Hartigh,[1] Veerle Geurts,[1] Lise Mangiante,[3] Lisa Lap,[4] Antonella F.M. Dost,[1,2] Joep Beumer,[1,2,18] Sonja Levy,[5] Rachel S. van Leeuwaarde,[6] Wenzel M. Hackeng,[7] Kris Samsom,[8] Catherine Voegele,[3] Alexandra Sexton-Oates,[3] Harry Begthel,[1] Jeroen Korving,[1] Lisa Hillen,[4] Lodewijk A.A. Brosens,[7] Sylvie Lantuejoul,[9,10] Sridevi Jaksani,[11] Niels F.M. Kok,[12] Koen J. Hartemink,[12] Houke M. Klomp,[12] Inne H.M. Borel Rinkes,[13] Anne-Marie Dingemans,[14,15] Gerlof D. Valk,[6] Menno R. Vriens,[13] Wieneke Buikhuisen,[16] José van den Berg,[8] Margot Tesselaar,[5] Jules Derks,[14] Ernst Jan Speel,[4] Matthieu Foll,[3] Lynnette Fernández-Cuesta,[3,*] and Hans Clevers[1,2,18,20,*]

[1]Hubrecht Institute, Royal Netherlands Academy of Arts and Sciences (KNAW) and UMC Utrecht, 3584 CT Utrecht, the Netherlands
[2]Oncode Institute, Hubrecht Institute, 3584 CT Utrecht, the Netherlands
[3]Rare Cancers Genomics Team (RCG), Genomic Epidemiology Branch (GEM), International Agency for Research on Cancer/World Health Organisation (IARC/WHO), 69007 Lyon, France
[4]Department of Pathology, GROW School for Oncology and Reproduction, Maastricht University Medical Centre, 6229 ER Maastricht, the Netherlands
[5]Department of Medical Oncology, Netherlands Cancer Institute, 1066 CX Amsterdam, the Netherlands
[6]Department of Endocrine Oncology, University Medical Center Utrecht, 3584 CX Utrecht, the Netherlands
[7]Department of Pathology, University Medical Center Utrecht, Utrecht University, 3584 CX Utrecht, the Netherlands
[8]Department of Pathology, Netherlands Cancer Institute, Amsterdam 1066 CX, the Netherlands
[9]Department of Biopathology, Pathology Research Platform- Synergie Lyon Cancer- CRCL, Centre Léon Bérard Unicancer, 69008 Lyon, France
[10]Université Grenoble Alpes, Grenoble, France
[11]Hubrecht Organoid Technology, Utrecht 3584 CM, the Netherlands
[12]Department of Surgery, Netherlands Cancer Institute, Amsterdam 1066 CX, the Netherlands
[13]Department of Endocrine Surgical Oncology, University Medical Center Utrecht, Utrecht 3508 GA, the Netherlands
[14]Department of Pulmonary Diseases, GROW School for Oncology and and Reproduction, Maastricht University Medical Centre, Maastricht, the Netherlands
[15]Department of Pulmonary Medicine, Erasmus MC Cancer Institute, University Medical Center, Rotterdam 3015 GD, the Netherlands
[16]Department of Thoracic Oncology, Netherlands Cancer Institute, Amsterdam 1066 CX, the Netherlands
[17]These authors contributed equally
[18]Present address: Roche Pharmaceutical Research and Early Development, Basel, Switzerland
[19]Present address: European Molecular Biology Laboratory (EMBL) Barcelona, Barcelona, Spain
[20]Lead contact
*Correspondence: talya.dayton@embl.es (T.L.D.), fernandezcuestal@iarc.who.int (L.F.-C.), h.clevers@hubrecht.eu (H.C.)
https://doi.org/10.1016/j.ccell.2023.11.007

SUMMARY

Neuroendocrine neoplasms (NENs) comprise well-differentiated neuroendocrine tumors (NETs) and poorly differentiated neuroendocrine carcinomas (NECs). Treatment options for patients with NENs are limited, in part due to lack of accurate models. We establish patient-derived tumor organoids (PDTOs) from pulmonary NETs and derive PDTOs from an understudied subtype of NEC, large cell neuroendocrine carcinoma (LCNEC), arising from multiple body sites. PDTOs maintain the gene expression patterns, intra-tumoral heterogeneity, and evolutionary processes of parental tumors. Through hypothesis-driven drug sensitivity analyses, we identify ASCL1 as a potential biomarker for response of LCNEC to treatment with BCL-2 inhibitors. Additionally, we discover a dependency on EGF in pulmonary NET PDTOs. Consistent with these findings, we find that, in an independent cohort, approximately 50% of pulmonary NETs express EGFR. This study identifies an actionable vulnerability for a subset of pulmonary NETs, emphasizing the utility of these PDTO models.

INTRODUCTION

Neuroendocrine neoplasms (NENs) show features of neuroendocrine differentiation, have the highest incidence in the lung and gastroenteropancreatic (GEP) system, and comprise what are considered two distinct entities, neuroendocrine tumors (NETs) and neuroendocrine carcinomas (NECs). The latter are poorly differentiated, high-grade tumors with a median life expectancy of less than 1 year.[1] NECs are further subdivided into small cell NECs and large cell NECs (LCNECs). NENs are

distinguished from adenocarcinoma and squamous cell carcinomas by a combination of morphological features and expression of at least one of the three standard neuroendocrine markers: chromogranin A, synaptophysin, and CD56/NCAM. Morphological features of NETs include rosettes, solid nesting architecture, and trabeculae. NECs show sheet or nodular growth with extensive necrosis and apoptosis.[1]

Small cell NECs are most common in the lung. Small cell lung cancers (SCLCs) account for ~15% of all lung cancers and are better studied than other NECs. LCNEC is more common in the GEP. Irrespective of tissue site, guidelines for treating patients with LCNEC remain rudimentary. Whether the therapeutic guidelines for SCLC can be applied to patients with LCNEC is unclear.[2]

NETs are well-differentiated, predominantly low-grade tumors (G1 and G2). The WHO criteria for the diagnosis of low-grade NET is a maximum mitotic count of 10 mitoses per 2 mm^2 for pulmonary NETs, or a Ki67 positivity rate of less than 20% for GEP NETs.[1] Pulmonary NETs are referred to as typical carcinoids (TC) if G1 and atypical carcinoids (AC) if G2. Although low-grade NETs are generally associated with a favorable prognosis, up to 35% of patients with NETs present with metastases, leading to a significant drop in overall survival rates.[3] The 10-year disease-specific survival for patients with metastatic G2 pulmonary NETs is 18% and it is unknown what the best treatment strategy is for these patients.[4]

Molecular analyses of pulmonary NETs have identified three groups: less aggressive carcinoids A1 and A2, and more aggressive carcinoids B.[5,6] In their study, Alcala et al. identify a subgroup of pulmonary NETs termed supra-carcinoids, highly aggressive tumors with the histopathological profile of low-grade NETs but the molecular profile of LCNEC. Pointing to their clinical relevance, supra-carcinoids are associated with a lower 10-year overall survival compared to G1/G2 pulmonary NETs. Other analyses of pulmonary NENs have identified subsets of tumors with similar characteristics to supra-carcinoids and there are several published reports of well-differentiated pulmonary NETs showing features of high-grade disease.[7–10] Currently, little is known about the biology of supra-carcinoids.

The lack of a clear standard of care for patients with LCNEC or clinically aggressive NETs underscores a clinical unmet need.[4,11,12] Whereas SCLC research has benefited from multiple models of the disease, LCNEC and NET research has been hindered by a paucity of preclinical models to test hypotheses about potential therapeutic targets and mechanisms of progression for NENs.[13–18]

Patient-derived tumor organoids (PDTOs) are 3D cultures of tumor cells that can be expanded long-term and are representative of their parental tumor tissue.[19–22] To date, a handful of PDTOs has been derived from high-grade NENs including SCLC, pulmonary LCNEC, and G3 GEP NETs and NECs.[23–27] In this study, we establish a collection of NEN PDTOs, including PDTOs of low-grade pulmonary NETs (LNET) and of LCNEC from multiple tissue sites. We also describe short-term cultures of small intestine NETs (SINET) PDTOs. Through multi-omic and phenotypic analyses, we confirm the fidelity of NEN PDTOs to their parental tumors and show that they preserve intra-tumoral heterogeneity and active evolutionary processes. Using this platform, we uncover a potentially actionable therapeutic vulnerability in a subset of pulmonary NETs, suggesting that growth factor dependence may be a feature of these tumors that can be exploited for therapeutic benefit.

RESULTS

Establishment of patient-derived tumor organoids (PDTOs) of understudied NEN subtypes

To generate PDTO models of understudied NEN subtypes, tissue samples from patients undergoing surgical resection or biopsy for NET or LCNEC were obtained, subjected to enzymatic digestion, and the resulting cell suspensions embedded in basement membrane extract (BME) and submerged in culture medium (see STAR methods). When PDTOs formed, they were expanded and used for downstream analyses (Figure 1A).

A panel of 11 LNET (lung NET) and 6 LCNEC PDTO lines was generated (Table S1), along with short-term PDTO cultures (up to passage 4) of 9 small intestine NETs (SINETs). We also further characterized an LCNEC PDTO, LCNEC4, generated and reported in a previous study from our lab.[24] All LCNEC and LNET PDTOs showed long-term growth in culture (Figure 1B). One line derived from a metastasis with unknown primary, mLCNEC23 (metastasis of LCNEC23), was established from a fine needle biopsy, showing the feasibility of establishing LCNEC PDTOs from small amounts of patient material. Multiple pathologists confirmed the diagnosis of NET or LCNEC of samples included in this study. NEN PDTOs displayed a variety of morphologies, ranging from dense structures to grape-like cell clusters (Figures 1C and S1A). Consistent with differences in their malignancy and proliferation, LCNEC PDTOs were readily established (75%; 6 out of 8), while LNET PDTOs showed an estimated success rate of 37% (11 out of 30; growth beyond 4 passages and/or 1 year) (Figure S1B).

NEN PDTOs recapitulate disease-specific growth phenotypes

Through histopathological analyses of PDTOs (13 out of 27 samples) (Table S1), we showed that PDTOs captured the histological features of their matching tumor of origin (Figures 2A–2C and S2A–S2C). Immunohistochemical (IHC) staining for the neuroendocrine markers chromogranin A (CHGA), synaptophysin (SYP), and CD56/NCAM1 on NEN PDTOs confirmed their neuroendocrine origin (Figures 2B, S2B, and S2D). Successful subcutaneous xenotransplantation of 4 LCNEC PDTO lines into immunocompromised mice (27 out of 30 injections; Table S1) confirmed tumorigenicity. Xenografted tumors stained positive for at least 1 out of 3 neuroendocrine markers (Figures 2A–2C, S2E; Table S1) and were confirmed to be LCNEC by pathologist assessment based on morphology, NE marker staining, and Ki67 positivity (Table S1).

A distinguishing feature of low-grade NETs is their low proliferation index.[1] IHC staining for the proliferation marker, Ki67 showed similar numbers of Ki67+ cells per field of view in NEN PDTOs and their matched parental tumors (Figure 2C and S2C). In line with these data, all PDTOs presented *MKI67* expression levels within what has been reported in their respective histopathological type[5,28,29] (Figure 2D).

As expected, LCNEC and LNET PDTOs had distinct *in vitro* growth rates. The average number of days it took for PDTOs of tumors of different grades (G1, G2, or G3/LCNEC) to be

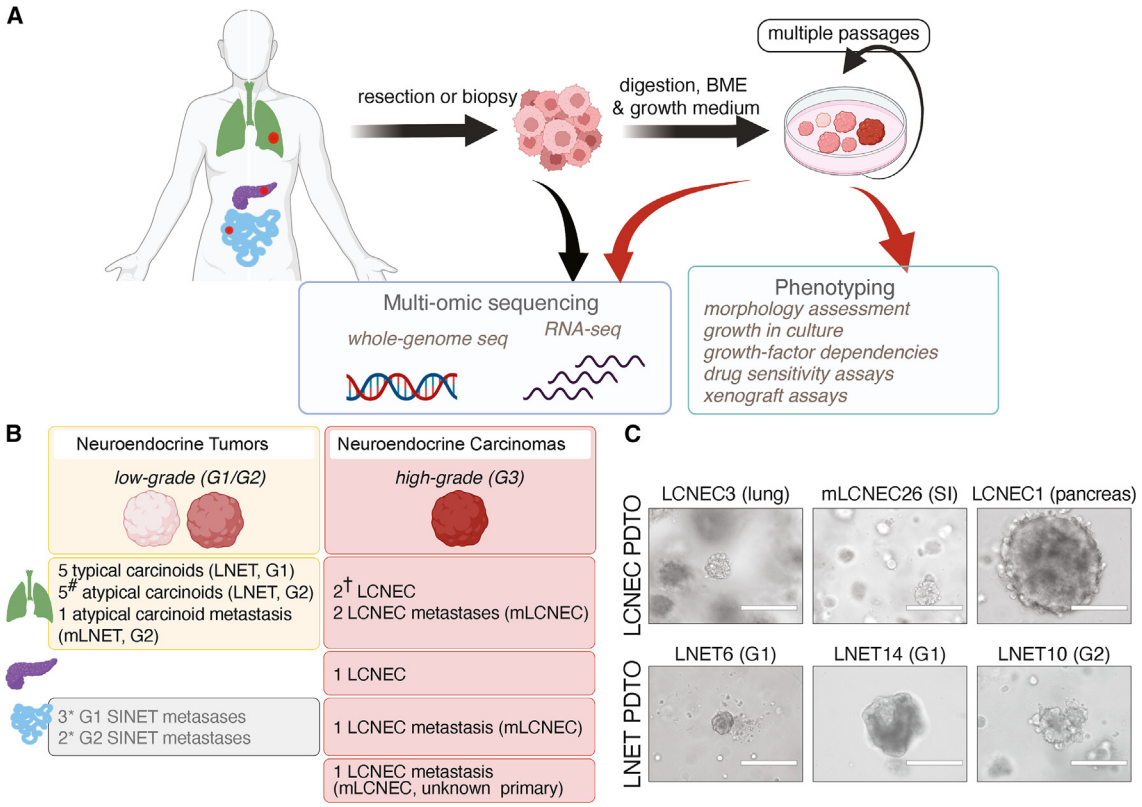

Figure 1. Establishment of NET and LCNEC patient-derived tumor organoids (PDTOs)

(A) Schematic of experimental design.

(B) Overview of established LNET and LCNEC PDTOs and short term SINET organoid cultures. LCNEC: large cell NEC; mLCNEC: metastasis of LCNEC; LNET: lung neuroendocrine tumor; mLNET: metastasis of LNET; SINET: small intestinal neuroendocrine tumor; G1: grade 1; G2: grade 2; G3: grade 3. LNET PDTOs without long-term growth were not included. #: 1 line from a presumed supra-carcinoid; *no growth beyond passage 4; †: 1 line previously reported.

(C) Representative bright-field images of NEN PDTOs. Scale bar: 200 μm. SI: small intestine. A and B. Made with biorender.com. See also Figure S1 and Table S1.

passaged five times (P5) revealed a clear pattern of decreased average time to P5 with increasing tumor grade (Figures 2E and 2F). We did not observe a temporal trend toward deceleration or acceleration of passage time in PDTO lines (Mann-Kendall test q-values > 0.18, Table S1). We did not perform this analysis on SINET PDTOs, as they could not be propagated past passage 4. Altogether, these data argue that PDTO culture did not alter the NEN subtype-defining phenotype of tumor growth rate. Of note, one LNET PDTO (LNET10) showed a remarkable growth rate compared to other LNETs (~150 days to P5, similar to LCNEC); as we will demonstrate in the following text, this tumor has other unique traits.

High-purity NEN PDTOs mirror the gene expression of their parental tumors

We assessed whether NEN PDTOs maintained the gene expression profiles of their parental tumors using bulk RNA sequencing (RNA-seq) (Figures 3A and S3A; Table S2). First, we examined the levels of expression for 3 canonical markers of neuroendocrine differentiation (*CHGA*, *CD56/NCAM1*, and *SYP*), and 3 neuroendocrine lineage transcription factors (*ASCL1*, *INSM1*, and *NEUROD1*)[13] (Figures 3B and S3B). For 15 out of the 21 parental-tumor PDTO families, expression levels for these markers were similar in PDTOs and their parental tumors and within the range of expression observed in reference samples (Figure 3B). Short-term SINET PDTO cultures had expression levels of the common therapeutic target, somatostatin receptor 2 (SSTR2), consistent with those observed in their parental tumors (Figure S3C).

The remaining 6 parental-tumor PDTO families, all derived from G1 or G2 LNETs, showed lower levels of expression for the examined neuroendocrine markers in the PDTO (Figure S3B). We performed IHC staining for the neuroendocrine marker CHGA in 3 of these LNET PDTOs and found that they consisted of CHGA+ tumor cells and undefined CHGA- cells (Figure S3D). We hypothesized that some PDTO lines contain both healthy and tumor cells, while others contain primarily tumor cells. To assess tumor purity of PDTOs, we categorized them as either "mixed" or "high-purity" based on a combination of molecular and IHC criteria (see STAR methods; Figure S3D; Table S3).

Transcriptomic analysis of high-purity PDTOs and their parental tumors, and a comparison with transcriptomes of NEN reference samples from previously published datasets, showed that they captured the molecular group of their parental tumor[5,28,30] (Figures 3C and 3D). Embedding and clustering by UMAP using genes representative of known molecular groups of pulmonary NENs and SINETs showed that PDTOs and their parental tumors clustered together with the reference NEN tissue samples of the expected molecular group. Although LCNEC1

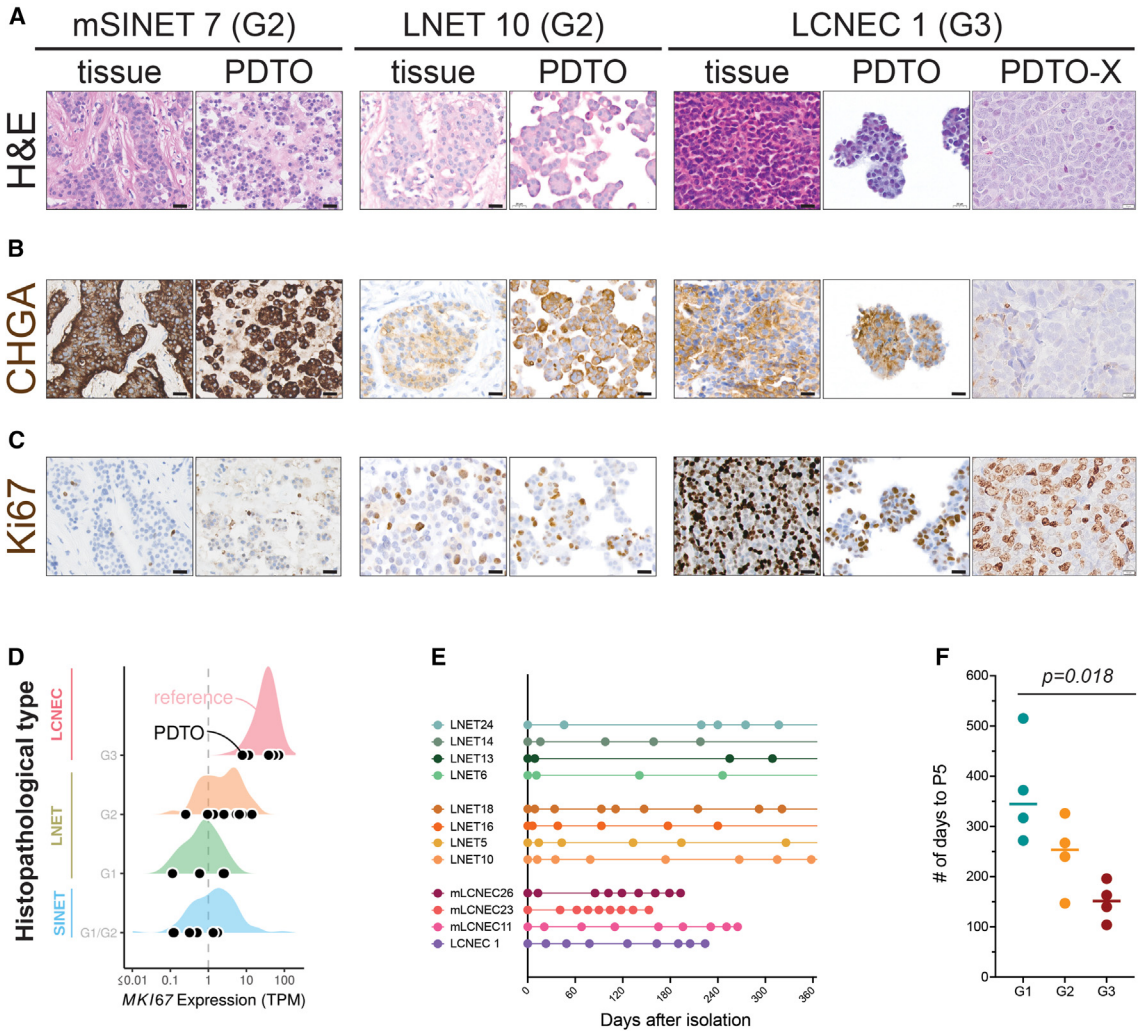

Figure 2. NET and LCNEC PDTOs retain histologic features and relative growth-rate of parental tumor subtypes

(A–C) Representative images of (A) hematoxylin and eosin (H&E) staining and immunohistochemical staining for (B) the neuroendocrine marker, chromogranin A (CHGA) and (C) the proliferation marker Ki67 of PDTOs, PDTO-xenotransplants (PDTO-X), and their parental tumor tissue. Scale bar: 20 μm except for PDTO-X images where scale bar is 10 μm mSINET: metastasis of small intestine NET; LNET: lung NET; LCNEC: large cell NEC.

(D) mRNA expression of *MKI67* in transcripts per million (TPM) in PDTOs and reference samples.[5,28,29] Black dots: PDTOs. Colored densities: distribution of reference sample expression values.

(E) Number of days in between each passage over the course of one year following isolation for LCNEC and LNET PDTOs. Each dot represents a passage. Data shown up to passage 8 or current passage number if lower than 8. mLCNEC: metastasis of LCNEC.

(F) Average cumulative number of days between date of isolation and passage 5 for PDTOs from tumors of different grades; p = 0.018, ANOVA. See also Figure S2 and Table S1.

and mLCNEC23 were from extrapulmonary LCNEC tumors (pancreas and unknown primary), both their parental tumors and PDTOs clustered with the reference pulmonary LCNECs, suggesting that LCNECs in different tissue sites share similar expression profiles.

The parental tumor and PDTOs from LNET10 clustered with LCNEC samples. From the reference datasets an additional three LNET samples, all previously reported as supra-carcinoids, also fell into the LCNEC cluster[5] (Figure 3C). Consistent with the hypothesis that LNET10 is a supra-carcinoid, the parental tumor and PDTOs displayed high expression of immune checkpoint genes and low expression of the putative prognostic marker, *OTP*[5,31,32] (Figure S3E). The clinical data of the patient with LNET10 was consistent with the diagnosis of supra-carcinoid: multiple metastases and recurrence following targeted therapy. The high *in vitro* growth rate for this PDTO (Figure 2E) is also consistent with this diagnosis.

To identify markers that distinguish PDTOs from their parental tumors, we performed Partial Least Squares (PLS) analyses of all PDTO lines and their matched parental tumor (Figure S3F). Gene set enrichment analysis (GSEA) on the identified markers showed that they are mostly immune-related, consistent with observations in PDTOs of other tumor types[33] (Figure S3G). These data support the notion that PDTOs contain the tumoral and epithelial components but not the stromal components of their parental tumors.

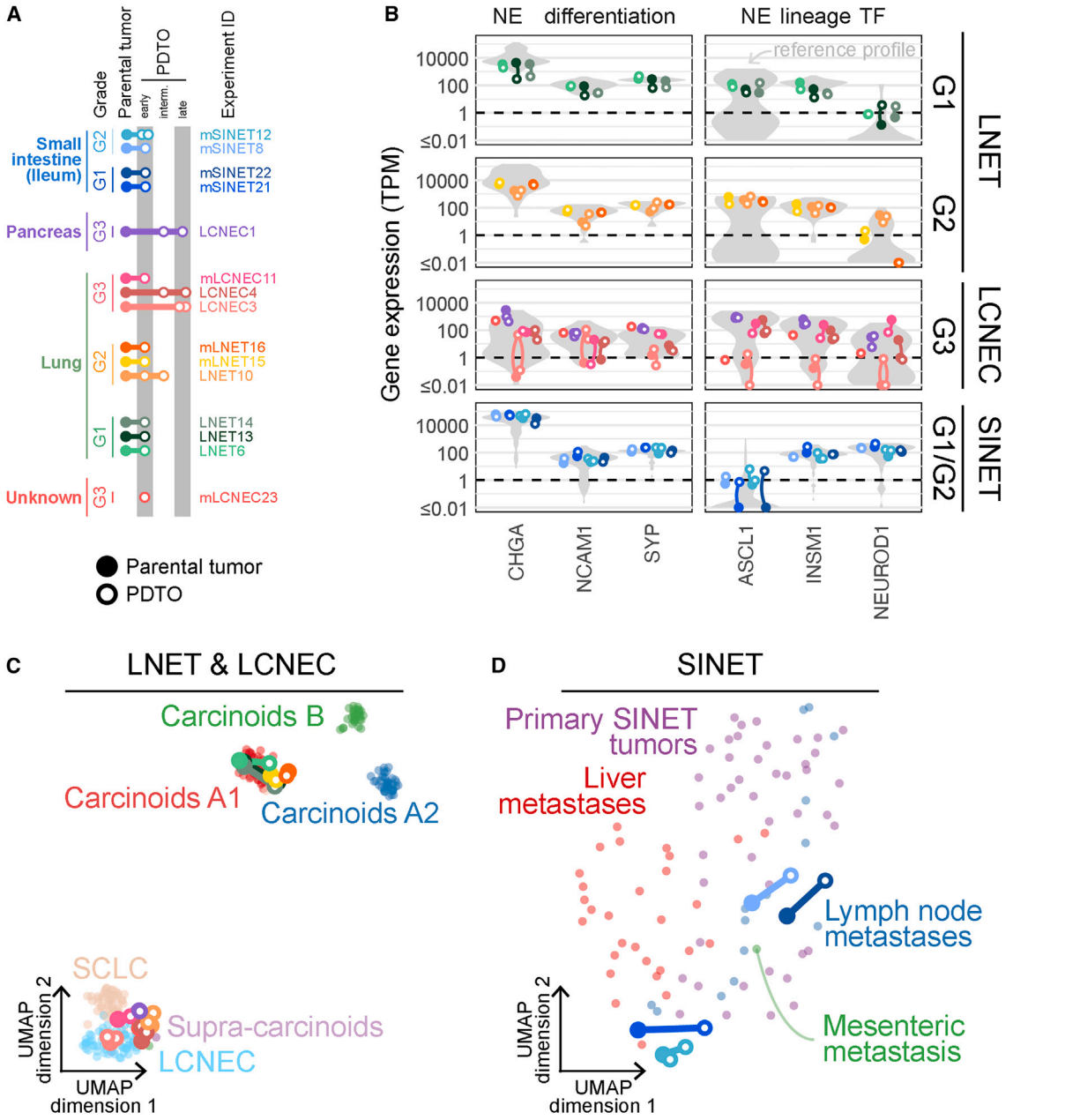

Figure 3. High-purity NEN PDTOs recapitulate the gene expression of original tumors

(A) Overview of high-purity PDTOs and parental tumors for which RNA-seq data were generated. Filled circles: parental tumors; empty circles: PDTOs (early passage: 1–3; intermediate passage: 4–7; late passage: 8+).

(B) Expression of neuroendocrine and transcription factor markers in PDTOs and parental tumors, in transcripts per million (TPM). Gray violin plots represent reference profiles with matching histological type and grade (n = 75 for G1 LNET, n = 40 for G2 LNET, n = 69 for LCNEC, n = 88 for SINET).

(C and D) Two-dimensional representation of the molecular profiles of PDTO within reference profiles from different molecular groups (point colors; n = 239 LNET & LCNEC, 88 SINET) using UMAP. (C) LNET and LCNEC for a set of 1055 core genes[5]; (D) small intestine NETs for a set of 519 genes (master regulators identified in Alvarez et al. Nature Genetics 2018). See also Figure S3 and Tables S2 and S3.

NEN PDTOs retain the genomic profile of their parental tumors

To determine whether NEN PDTOs recapitulate the genomic landscape of their parental tumors, we performed whole genome sequencing (WGS) in 10 parental-tumor PDTO families representing all tumor types and grades in the collection, and including multiple time points in culture for 2 LCNEC lines (Figures 4A and S4A; Table S4).

Tumor mutational burden (TMB) was similar between PDTOs and their parental tumor (Figures 4B and S4B). Consistent with previous observations, TMB was lower for NET than LCNEC (mean 1.26 and 11.5, respectively).[5,34–36] The spectrum of

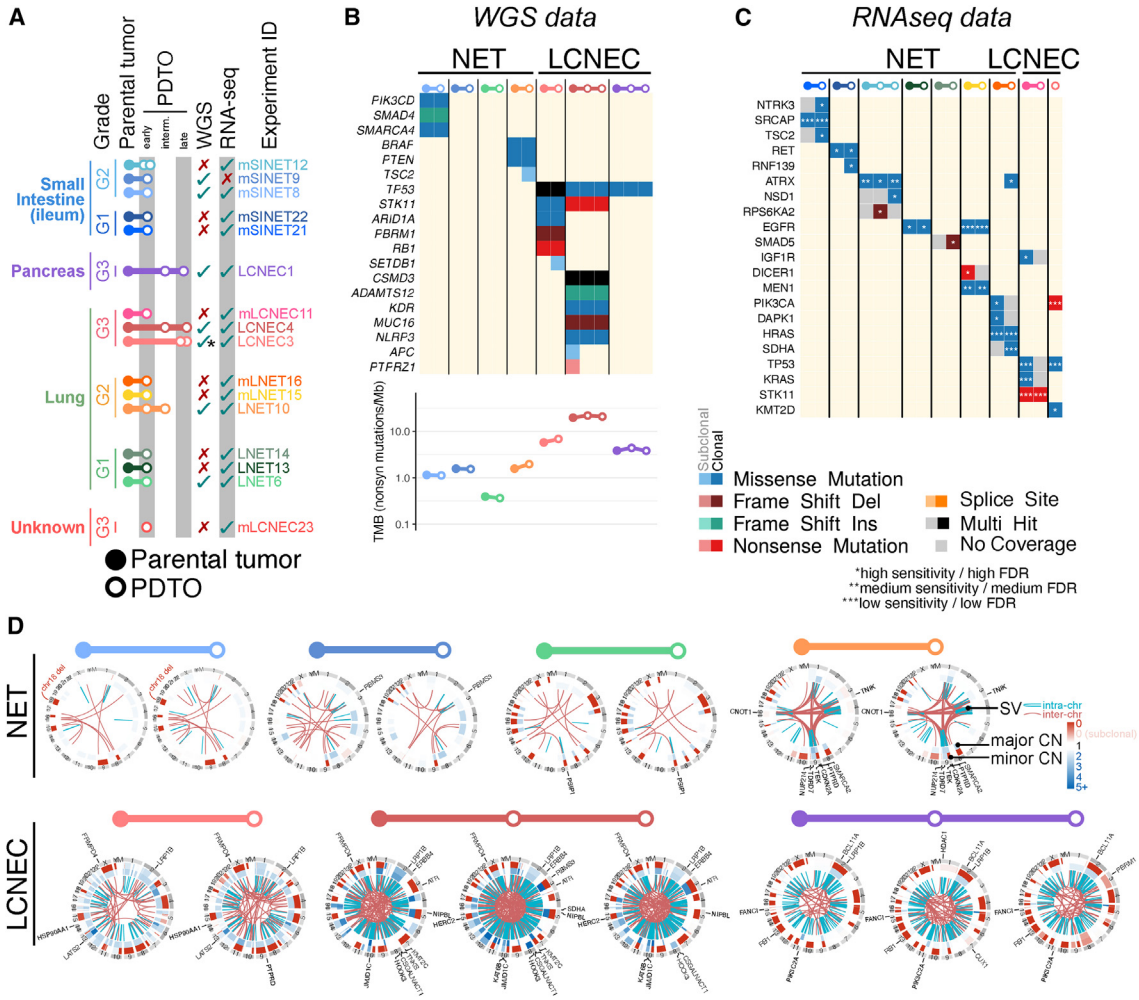

Figure 4. NEN PDTOs retain genomic features of parental tumors

(A) Overview of high-purity PDTOs and parental tumors for which whole genome sequencing (WGS) and/or RNA-seq data were generated. Filled circles: parental tumors; empty circles: PDTOs (early passage: 1–3; intermediate passage: 4–7; late passage: 8+). *LCNEC3: WGS data were generated for 1 passage, RNAseq data for 2 passages.

(B and C) Summary of putative pathogenic somatic alterations detected by (B) WGS or (C) RNA-seq in genes reported to be recurrently mutated in LCNEC, LNET, and SINET. Colors represent variant classes and clonality (light: subclonal; solid: clonal). In (B), the lower panel represents the Tumor Mutational Burden (TMB), the number of nonsynonymous mutations per megabase. In (C), light gray represents genes without enough coverage to detect variants. The EGFR mutation in LNET13, L135Q, has not been reported in the COSMIC database and is unlikely to be an oncogenic alteration. The EGFR mutation in mLNET15, G828E, COSMIC ID COSV51784752, has been reported in 4 samples and has unknown significance.

(D) Structural variants in PDTOs and parental tumors. Inner layer: chromosomal rearrangements; central layer: major copy number (CN); outer layer: minor CN. Structural variants damaging genes that have been previously reported as recurrently mutated in LCNEC, LNET, or SINET are annotated in black. Subclonal CN alterations (non-integer CN) are indicated with intermediate colors (e.g., light red for subclonal CN loss). See also Figure S4 and Table S4.

mutationally altered genes observed recapitulated genomic alterations previously reported in NENs.[5,7,28,34,36–41] NET PDTOs presented fewer single nucleotide variants (SNVs) and insertions and deletions (indels) in known driver genes than LCNEC PDTOs (average of 1.5 vs. 4), with SINET9 and LNET6 samples showing none (Figures 4B and S4B). For 5 out of 8 high-purity PDTO WGS profiles, the SNVs in putative driver genes observed in the parental tumors were also observed in the corresponding PDTO line, showing a high degree of concordance. In the remaining 3 high-purity PDTO lines, LNET10, LCNEC3, and LCNEC4, discordance between the PDTO and corresponding parental tumor was seen exclusively in subclonal alterations and in only up to 2 putative driver SNVs (Figure 4B). In the case of the 2 "mixed" LNET PDTO-parental tumor WGS profiles in our dataset, LNET2 and LNET5, we identified somatic driver mutations confirming that they contain tumoral tissue (Figure S4B).

To identify somatic variants in samples for which WGS had not been performed, we used RNA-seq data to call SNVs in genes previously found to be altered in NENs (Figures 4C and S4C). We identified 28+ unique, putatively oncogenic mutations (see STAR methods) in either the PDTOs, parental tumors, or both affecting *MEN1*, *ATRX*, *HRAS*, *TSC2*, *PIK3CA*, and *STK11*[5,28,34,36] (Figure S4C).

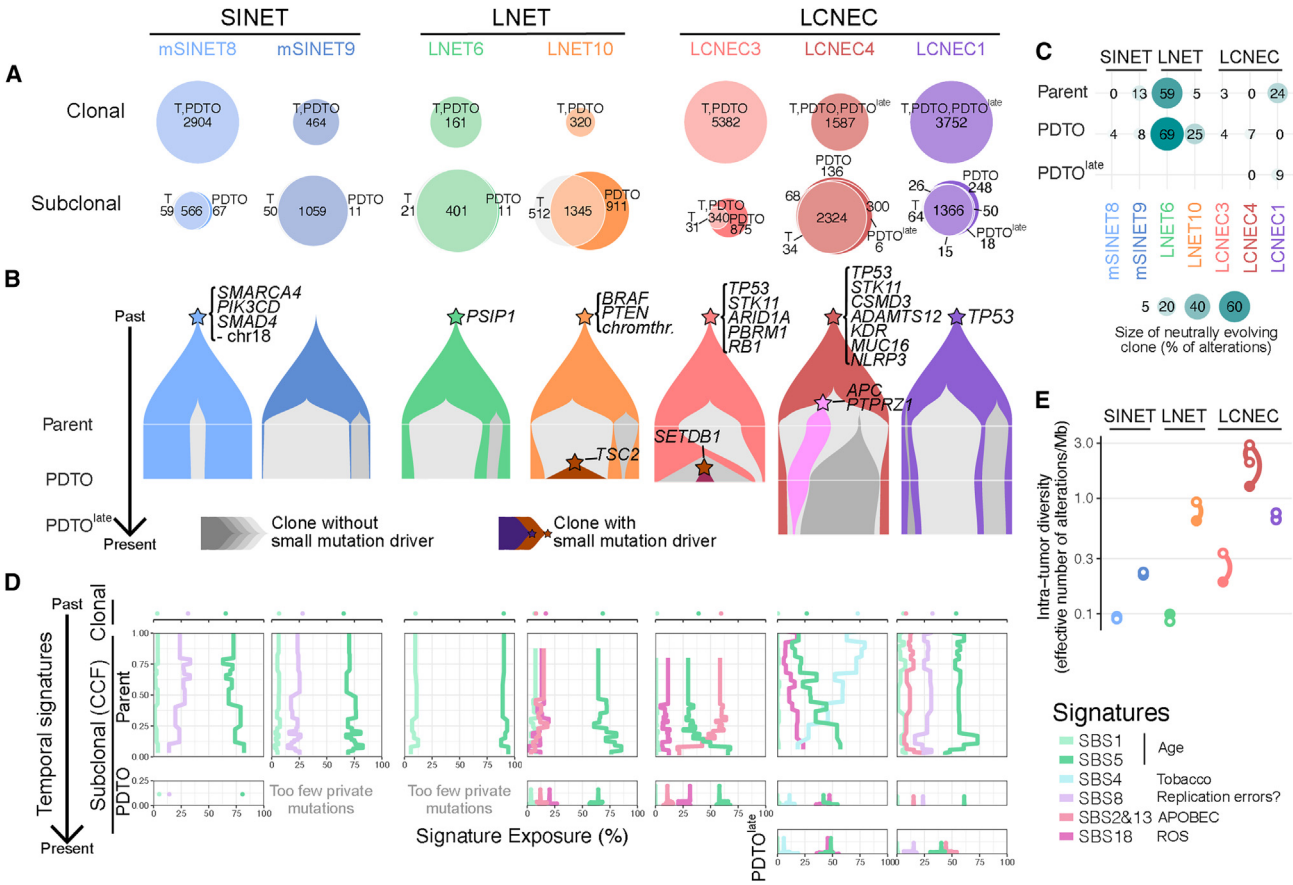

Figure 5. NEN PDTOs recapitulate the intra-tumor heterogeneity of the parental tumor

(A) Venn-Euler diagrams of shared and private clonal (top) and subclonal (bottom) somatic small variants.

(B) Fish plots showing clonal reconstruction of tumor and organoid.

(C) Mode of evolution, measured as the size of the neutrally evolving clone in percentage of subclonal alterations (see STAR methods).

(D) Temporal mutational signatures, measured as the signature exposure (the percentage of mutations belonging to each signature), in clonal small variants (top), subclonal small variants present only in the parental tumor (middle), and those only present in the PDTO (bottom). The vertical axis corresponds to the cancer cell fraction (CCF), a proxy for the age of the mutation (older alterations: top; high CCF, recent alterations: bottom; low CCF).

(E) Intra-tumor genetic diversity, the effective number of alterations per Mb (see STAR methods). In (A), (B), and (D), columns correspond to PDTO/parent families. See also Figure S5.

When coverage of the region of interest for the relevant mutations and samples was sufficient, the mutations identified in the tumor were also found in the corresponding PDTO (10/28 mutations and for 9/11 PDTO parental-tumor pairs) (Figures 4C and S4C). We identified the oncogenic *HRAS* G13D mutation in all samples from LNET16, including the primary pulmonary NET, its matched metastasis, and the corresponding tumor- and metastasis-derived PDTOs. We also identified a somatic mutation in *MEN1,* the most commonly altered gene in pulmonary NETs, in both the tumor and PDTO from mLNET15.[5,34,38] The parental tumor sample from mLCNEC11 was found to carry the oncogenic *KRAS* G12V mutation and the PDTO of mLCNEC23 a predicted oncogenic mutation in the *TP53* gene.

At the level of copy number alterations and structural variants (SVs), PDTOs captured both focal events and large-scale chromosomal aberrations (Figures 4D and S4D). As examples of the former, we observed *RBMS3* translocations in SINET9, and a *PSIP1* inversion and a large deletion in LNET6. For the latter, we observed a potential chromothripsis event in LNET10 affecting chromosomes 1, 3, 4, 9, and 16, whole-genome doubling in LCNEC4, and chromosome 18 loss—a known event observed in more than 60% of SINETs—in SINET8.[42,43] Overall, the patterns of copy number alterations and SVs were conserved between parental tumors and PDTOs, and were consistent with patterns previously observed in NENs.

Organoids capture the intra-tumor heterogeneity and evolutionary processes of their parental tumors

To determine whether PDTOs capture the fine-scale genetic makeup of their parental tumors, we performed clonal deconvolution and evolutionary analyses. PDTOs recapitulate the ratio of clonal and subclonal alterations of each tumor type (Figures 5A, S5A, and S5B), with NETs having predominantly subclonal alterations (from ~400 to ~3200), and LCNECs having predominantly clonal alterations (from ~1500 to ~5300). Subclonal alterations were predominantly present at similar cancer cell fractions in the parental tumor and matched PDTOs, and even alterations present in only a small percentage of parental tumor cells were detected in

the PDTO (Figure S5A). As expected, concordance of subclonal mutations between PDTOs and parental tumors was highest in the low-grade NETs (<11% of private alterations in mSINET8, mSINET9, and LNET6). An exception to this was LNET10, the putative supra-carcinoid, which showed more substantial subclonal differences (~40% of private alterations).

These analyses showed that PDTOs preserve the main subclones of their parental tumor (Figures 5B and S5C). In concordance with their lower grade and lower passage time, and consistent with past and present neutral evolution, we did not identify known driver alterations in subclones of SINETs or LNET6 PDTOs but detected neutrally evolving subclones in both parents and PDTOs (MOBSTER method,[44]; Figures 5C and S5D). Interestingly, supra-carcinoid LNET10 had multiple clonal driver mutations (*BRAF*, *PTEN*, a chromothripsis event affecting many genes), consistent with past linear evolution. This sample also had a subclonal *TSC2* mutation that was found at high frequency in the PDTO but was either absent or below the detection limit in the parental tumor, an observation consistent with a possible ongoing selective sweep. LCNEC1, 3, and 4 also show signs of past linear evolution, and possibly ongoing natural selection, due to the presence at low frequency of driver mutations in LCNEC3 (*SETDB1*) and LCNEC4 (*APC* and *PTPRZ1*) PDTOs. These data suggest that both past and present evolution under natural selection are captured by PDTOs.

We reasoned that the mutations that were private to the PDTO could have been generated either by the same mutational processes observed in the parental tumor or by new mutational processes specific to the PDTO and/or the culture conditions. To determine which of these was true, we used the TrackSig method[45] to reconstruct the temporal trajectory of mutational signatures in tumors and PDTOs.

Mutations appearing in the PDTOs were not only generated by the same processes that were active in the parental tumors, but they also reflected recent shifts in sources of mutation (Figures 5D and S5E). For instance, a signature associated with reactive oxygen species, single base substitution 18 (SBS18), was detected in LCNEC3 and LCNEC4 subclonal alterations and was also found in their PDTOs. Even the quasi-absence of the tobacco smoking-associated SBS4 in LCNEC4 PDTO cells is consistent with a recent drastic decline in this signature in the parental tumor (from 73% of clonal alterations to 18% of "recent" alterations). This shows that PDTOs preserve the endogenous mutational processes operating in the parental tumors.

Finally, we investigated whether PDTOs presented stable levels of intra-tumoral heterogeneity. Interestingly, even late passage PDTOs harbored levels of genetic diversity similar to those observed in parental tumors (Figures 5E and S5F). No sample presented any substantial loss of diversity: LNET6, a low-grade tumor, presented the largest loss but it was minimal (less than 0.02 effective alteration/Mb), potentially indicating that a fraction of tumor cells did not survive in culture. These data argue that PDTOs globally preserve the evolutionary processes at work in their parental tumors: the subtle balance in parental tumors between processes generating genetic diversity, such as mutational processes, and those reducing genetic diversity, such as natural selection and genetic drift, are maintained.

Hypothesis-driven drug sensitivity testing in PDTOs from clinically aggressive NENs

PDTOs have been shown to have predictive value in cancer therapy.[21,46–50] We performed dose titration assays to examine the effects of several drugs on 5 LCNEC PDTOs. Given its aggressive clinical course and the evidence that it represents a supra-carcinoid, we included LNET10 PDTOs in these assays.

We first tested the response of organoids to the taxane, paclitaxel, and to the mTOR inhibitor, everolimus. In the clinic, paclitaxel is sometimes used in combination with carboplatin to treat patients with pulmonary LCNEC.[38] Everolimus is an approved therapy for low-grade NETs also being tested for the treatment of NECs.[13,51] We observed differential drug responses of individual PDTO lines to these compounds, with 4 out of 6 of the tested PDTOs showing some response to both drugs (Figures 6A, S6A, and S6B).

We were also interested in determining whether PDTOs could predict patient response to targeted therapies. WGS analysis of the tumor tissue and matched PDTOs from the putative supra-carcinoid, LNET10, identified a *BRAF* V600E mutation (Figure 4B). Some patients with *BRAF*-mutated tumors show clinically significant responses to combined treatment with BRAF and MEK inhibitors.[52,53] We tested the response of LNET10 PDTOs to both single-agent and combination treatment with the BRAF inhibitor, dabrafenib and the MEK inhibitor, trametinib (Figures S6C–S6E). As a comparison, we tested the response of *BRAF*-wildtype mLCNEC23 PDTOs to these inhibitors. Whereas mLCNEC23 PDTOs were resistant to both single-agent treatments and their combination, *BRAF*-mutant LNET10 PDTOs were sensitive to all treatments (area under the fitted dose response curve—AUC—for combination, 186 and 96, respectively). We did not observe an improved response of LNET10 PDTOs to combination treatment compared to single-agent treatments. Notably, neither drug nor their combination was able to kill all the cells in LNET10 PDTOs. Anecdotally, treatment of the respective LNET10 patient with this same drug combination led to an initial response followed by tumor relapse and resistance to treatment.

We next sought to identify new therapeutic opportunities for LCNEC patients. Small cell lung cancer (SCLC), the best-studied subtype of NEC,[54] can be subdivided into molecular groups defined by the differential expression of lineage transcription factors: *ASCL1*, *NEUROD1*, and *POU2F3*.[55] Preclinical studies suggest that tumors belonging to different SCLC molecular groups have distinct therapeutic vulnerabilities.[55–60] *ASCL1* and *NEUROD1* are highly expressed in some LCNEC tumors, in the majority of our LCNEC PDTOs, and in LNET10 PDTOs[36,61–63] (Figure 3B). To determine whether these PDTOs show sensitivities consistent with those identified for *ASCL1*-high or *NEUROD1*-high SCLC, we tested their response to therapies specific for these SCLC molecular groups: the BCL2 inhibitor, navitoclax, and the Aurora kinase inhibitor, alisertib, respectively[56,59,60] (Figures 6B, S6E, and S6F). While the tested lines did not show a response to treatment with alisertib, we noted a differential response of PDTOs to navitoclax. In agreement with what has been observed for SCLC, PDTOs with high *ASCL1* expression were sensitive to treatment with navitoclax, while lines with low *ASCL1* expression were resistant to the treatment. Although the sample size did not provide sufficient power to definitively

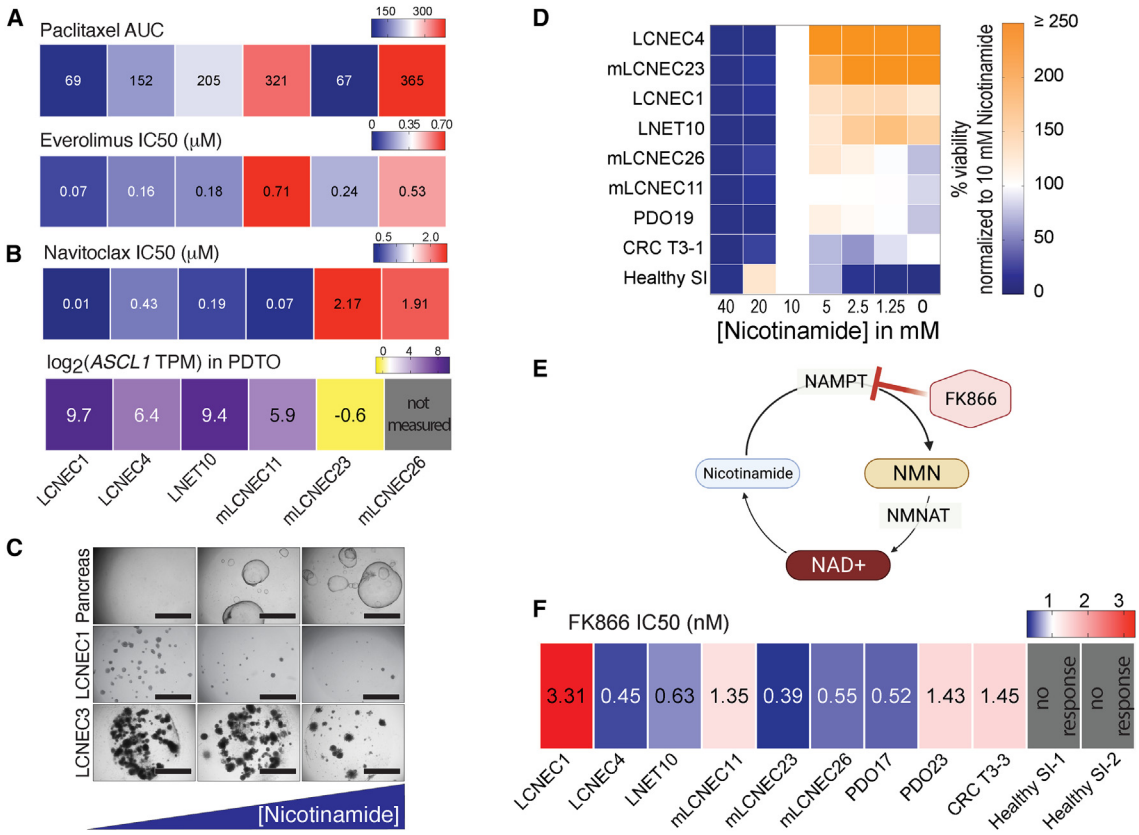

Figure 6. Hypothesis driven drug sensitivity testing in PDTOs from clinically aggressive NENs reveals therapeutic vulnerabilities to approved therapies

(A) Heatmap showing area under the curve (AUC) values for paclitaxel and IC50 values for everolimus of tested PDTO lines. For paclitaxel, the dose-response curve did not allow for IC50 value calculation and AUC is reported instead. Dose-response curves shown in Figures S6A and S6B.

(B) Top: Heatmap showing IC50 values for the BCL-2 inhibitor, navitoclax, of PDTOs. Bottom: Heatmap showing expression of *ASCL1* (in log2 of TPM) in PDTOs.

(C) Brightfield images of organoid outgrowth from single cells in media containing increasing concentrations of nicotinamide. Pictures of normal pancreas organoids (top panel) taken on day 7 after plating. Pictures of LCNEC organoids (bottom two panels) taken on day 26 after plating. Concentrations from left to right: 0 mM, 10 mM, 20 mM. Scale bars: 2,000 μm. Magnification: 2×.

(D) Quantification of organoid outgrowth from single cells in different concentrations of nicotinamide for LNET 10, 5 LCNEC PDTO lines, colorectal cancer (CRC) PDTO line (T3-1), pancreatic ductal adenocarcinoma line (PDO19), and healthy small intestine (SI) organoids. Cell number was measured by Cell-titer Glo ATP assay. Data are shown relative to outgrowth of the same line in 10 mM nicotinamide.

(E) Diagram depicting NAD+ salvage biosynthesis pathway. Created using biorender.com.

(F) Heatmap showing IC50 values of NEN PDTO lines, a colorectal cancer PDTO line (CRC T3-3), 2 pancreatic ductal adenocarcinoma PDTO lines (PDO17, PDO23), and 2 healthy SI lines for the NAMPT inhibitor, FK866. See also Figure S6.

prove the association, high expression of *BCL2* also appeared to be predictive of a low IC50 value for navitoclax (Spearman's $\rho = -0.8$, one-sided rank test p value = 0.067). These data point to *ASCL1* expression in NENs as a potential general biomarker for therapeutic response to BCL2 inhibitors.

During the medium optimization phase of our study, NEN PDTOs showed the best outgrowth in medium lacking nicotinamide (Figure 6C). This was unexpected because nicotinamide is an essential component of the medium used to culture multiple kinds of organoids.[19,64] To quantitatively assess the effect of nicotinamide on PDTOs, we tested the outgrowth efficiency of single cell suspensions derived from LCNEC and LNET10 PDTOs, from PDTOs of other tumor types (colorectal cancer and pancreatic ductal adenocarcinoma), and from healthy tissue derived organoids, in different concentrations of nicotinamide (Figure 6D). As previously observed, 10 mM nicotinamide was optimal or near optimal for outgrowth of the healthy tissue organoid lines and the colorectal cancer PDTO line. This was not the case for NEN PDTOs, where 4 out of 6 NEN PDTOs showed the best outgrowth at either the lowest concentration of nicotinamide, 1.25 mM, or in its complete absence.

Nicotinamide is a precursor of oxidized nicotinamide adenine dinucleotide (NAD+).[65] We speculated that the outgrowth inhibition of nicotinamide on NEN PDTOs implicates a sensitivity of NENs to drugs that influence the conversion of nicotinamide to NAD+. To test this possibility, we exposed LCNEC PDTOs, LNET10 PDTOs, PDTOs of other tumor types (colorectal cancer and pancreatic ductal adenocarcinoma), and healthy intestinal tissue organoids to FK866, an inhibitor of nicotinamide phosphoribosyltransferase (NAMPT), the enzyme that catalyzes the rate-limiting step in the NAD+ salvage pathway[65] (Figures 6E–6F and S6G). Consistent with our media assays, while healthy

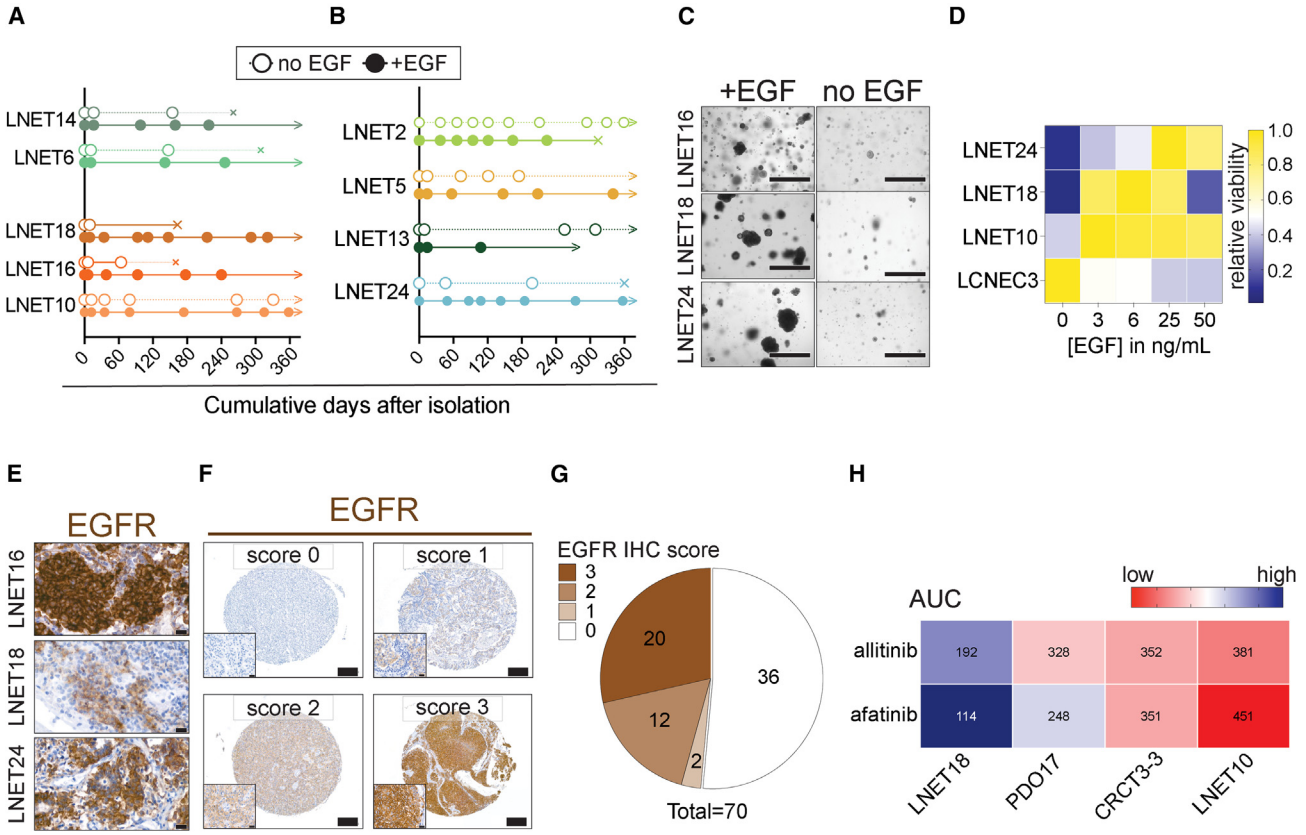

Figure 7. Lung NET PDTOs are dependent on EGF and EGFR expression is common in lung NETs

(A and B) Number of days between passages spanning one year (A) following isolation in medium with or without EGF, or (B) following isolation in medium without EGF or thawing into medium with EGF. Each dot represents a passage.

(C) Brightfield images showing growth of LNET PDTOs in the presence or absence of EGF, 31 days (LNET16), 42 days (LNET18), or 75 days (LNET24) after plating. Scale bars: 1,000 μm. Magnification: 4×.

(D) Quantification of organoid outgrowth from single cells in different concentrations of EGF for 3 LNET PDTOs and 1 LCNEC PDTO. Cell number was measured by Cell-titer Glo ATP assay. Data are shown relative to outgrowth of the same line in no EGF and normalized to highest viability value.

(E) Immunohistochemical (IHC) staining for the EGF receptor, EGFR, in parental tumor tissue for the PDTOs in C. Scale bar: 20 μm.

(F) Representative tissue microarray (TMA) cores containing pulmonary NET samples stained for EGFR. An example of each EGFR IHC intensity score is shown (0, negative; 1, weak; 2, medium; 3, strong). See Table S5 for a summary of scores and percent positive tumor cells for TMA cores and tumors. Scale bars: 200 μm; inset: 20 μm.

(G) Distribution of EGFR IHC intensity scores for 70 pulmonary NETs from two different TMAs. Each tumor was represented by 3 cores.

(H) Heatmap showing sensitivity of LNET 18, LNET 10, PDO17, and CRCT3-3 to the EGFR inhibitors allitinib and afatinib, as measured by area under the curve (AUC). Numerical values for AUC are shown. Red indicates high AUC values, blue indicates low AUC values. The dose-response curve did not allow for IC50 value calculation and AUC is reported instead. PDO17: pancreatic ductal adenocarcinoma PDTO, CRC T3-3, colorectal cancer PDTO. See also Figure S7 and Table S5.

tissue organoids showed no response to treatment with FK866, 4 out of 6 NEN PDTO lines showed subnanomolar IC50 values. In all cases, the IC50 values were below the steady state plasma concentrations for FK866 (14 nM) reported in a Phase I clinical trial, suggesting clinical relevance of these results.[66,67] Pancreatic ductal adenocarcinoma and colorectal cancer PDTOs showed IC50 values for FK866 within the same range as the tested NEN PDTO lines. These results indicate that PDTO media requirements can be used to identify potential therapeutic vulnerabilities.

A subset of lung NET PDTOs are dependent on EGF and expression of the EGF receptor is common in lung NETs

To identify dependencies in NEN PDTOs, we tested the requirement for growth factors commonly used in organoid culture: EGF or FGF7 and FGF10. When sufficient tissue was available, we cultured a portion of the cell suspension in base NEN PDTO media, a portion in media supplemented with FGF7 and FGF10, and a portion in media supplemented with EGF. Consistent with the notion that high-grade tumors acquire growth-factor independence, 5 out of 7 LCNEC PDTOs showed no discernible difference in growth with the additional growth factors (Figure S7A).

Pulmonary NET PDTOs appeared to be EGF-dependent. Starting at the time of organoid isolation, we directly compared the outgrowth of five LNET PDTOs in media containing EGF and media lacking EGF (Figure 7A). In all cases, better outgrowth was observed in media containing EGF. In 4 out of 5 cases, the omission of EGF precluded growth beyond 3 passages. The short-term PDTO cultures of SINETs did not grow beyond passage 4 and were not tested for growth factor dependencies.

Given that LNET PDTOs were dependent on EGF, we asked whether LNET PDTO lines that had shown suboptimal growth in medium without EGF might be similarly dependent on EGF. We thawed frozen vials of 4 LNET PDTO lines (LNET2, LNET5, LNET13, and LNET24), directly into media containing EGF and compared their outgrowth over time to the outgrowth dynamics we had observed for the same lines in media without EGF (Figure 7B). 2 out of these 4 PDTO lines (LNET5 and LNET24), could be expanded more times within a 1-year time frame than when they had been grown for the same length of time without EGF. LNET24 displayed the most striking difference; without EGF it could only be passaged 3 times, but with the addition of EGF, it was passaged 7 times. In line with these observations, withdrawal of EGF from lines grown in EGF media, or addition of EGF to lines that had been grown in the absence of EGF, revealed improved expansion in the EGF-containing media (Figure 7C).

To quantitatively assess EGF-dependency in LNET PDTOs, we performed an EGF dose response outgrowth assay (Figure 7D). EGF improved the expansion of LNET18 and LNET24 PDTOs in a dose-dependent manner. While 2 out of 3 LNET PDTOs showed similar expansion at 25 ng/μL and 50 ng/μL, LNET18 PDTOs showed reduced expansion at 50 ng/μL of EGF compared to even 3 ng/μL of EGF. It is possible that for LNET18, at the highest concentrations of EGF, the internalization rate for the EGF receptor, EGFR, exceeded the rate at which it could be recycled back to the plasma membrane. Indeed, culturing head and neck cancers PDTOs at low EGF concentrations led to increased expression of membrane EGFR.[68] LCNEC3 PDTOs were not dependent on EGF, and we noted the best expansion in the absence of EGF. Given that LNET10 tumor tissue and PDTOs harbor a *BRAF*^{V600E} mutation, which leads to EGF-independent activation of the MAPK pathway, we were surprised to observe increased expansion of LNET10 PDTOs in all of the tested EGF concentrations compared to without EGF. Adaptive feedback activation of MAPK signaling has been observed in *BRAF*-mutant colon cancers treated with BRAF inhibitors, suggesting that EGF-mediated MAPK activation can promote the growth of EGFR-expressing *BRAF*-mutant tumors.[69,70]

We next analyzed RNA-seq data from PDTOs and parental tumors and from previously published datasets of pulmonary NET tissue[5] (Figure S7B). *EGFR* expression was present in most tumors and PDTOs in these datasets. IHC staining for EGFR confirmed membrane EGFR protein expression in 11 out of 13 LNET parental tumors (Figures 7E and S7C; Table S5). In line with the observation that LNET2 PDTOs were not dependent on EGF and that LNET19 PDTOs could not be propagated long-term in EGF-containing media, EGFR staining of LNET2 and LNET19 parental tumor tissue was negative. mLNET15 and LNET20 parental tumor tissue showed some staining for EGFR but their PDTO growth stopped at passage 3, suggesting that factors other than EGF contribute to *in vitro* growth of some EGFR-expressing tumors.

To ask whether EGFR expression is a common feature of pulmonary NETs, we performed IHC staining for EGFR on pulmonary NET tumor tissue microarrays containing a total of 216 cores from 73 pulmonary NETs (Figure 7F). We assigned each stained core a membrane EGFR staining intensity score and used this to assign a score to the pulmonary NETs on the array. 48% of tumors expressed membrane EGFR, most of which showed very strong staining (Figure 7G). Altogether, these data show that a subset of close to half of pulmonary NETs expresses membrane EGFR.

Our data imply that some pulmonary NETs might be sensitive to treatment with EGFR inhibitors. To begin to test this possibility, we treated 1 EGF-independent (LNET10) and 1 EGF-dependent (LNET18) PDTO line with EGFR inhibitors (Figure 7H). As we did not observe activating mutations in EGFR in our LNET PDTOs, we chose EGFR inhibitors that target the wild-type receptor, allitinib and afatinib. As a reference for EGFR sensitivity, we simultaneously tested 2 PDTO lines which have previously been shown to be respectively sensitive (PDO17) and resistant (CRC T3-3/P3.T2.1) to treatment with afatinib.[71,72] Consistent with the observation that it was dependent on EGF for growth in culture, LNET18 PDTOs showed the lowest AUC values of all the tested lines (LNET18 192 and 227, PDO17 328 and 248 for allitinib and afatinib, respectively). LNET10 PDTOs, which have a downstream activating mutation, and CRC T3-3 PDTOs both had AUC values > 300. EGF-dependent LNET18 PDTOs were also sensitive to inhibition of EGFR downstream signaling, via treatment with the MEK inhibitor, trametinib (Figure S7D). We also tested LCNEC1 and LNET10 and found both lines were sensitive to MEK inhibition, indicating that MAPK signaling might be important for some NENs independent of tumor grade. Collectively, these data are consistent with the notion that a subset of pulmonary NETs is dependent on EGF growth-factor signaling and provide a rationale for further investigating the potential for treating these tumors with EGFR or MAPK-targeted therapies.

DISCUSSION

In this study, we established a biobank of human NEN PDTOs that fully recapitulates the spectrum of malignancy observed for NENs, encompassing both slow growing tumors and highly proliferative, metastatic carcinomas. Our biobank includes models of an understudied subtype of high-grade NEN, LCNEC, PDTOs of low-grade pulmonary NETs, and a PDTO derived from a supra-carcinoid, a clinically aggressive pulmonary NET. Other NEN organoid biobanks were recently reported.[25,26] These biobanks contain primarily GEP NECs or GEP G3 NETs and lack models of low-grade NETs and pulmonary LCNEC. Lung NENs account for 25% of all NENs and even low-grade pulmonary NETs show a significant rate of metastasis.[3,13] Thus, the inclusion of low-grade pulmonary NET PDTOs in our collection represents a valuable addition to the cell models currently available for NEN research. The development of these models enabled the clinically relevant discovery that a subset of pulmonary NETs is dependent on EGF. Altogether, our NEN PDTO biobank will provide opportunities for investigating carcinogenesis and therapeutics across the broad spectrum of aggressiveness for NENs.

A hurdle in the development of NET PDTOs has been the lack of clarity regarding their potential growth-factor dependencies. Our discovery of EGF dependence in some pulmonary NET PDTOs has significant clinical implications. Pulmonary NETs expressing membrane EGFR might respond to the therapies targeting EGFR or EGFR-mediated downstream signaling that are currently approved for the treatment of other tumor types. There are other reports of EGFR expression in pulmonary NETs, but

these studies were unable to demonstrate a functional role for receptor expression in promoting the growth or survival of these tumors.[73–76] Our data argue that EGFR expression is indicative of EGF-dependence. The patient population most likely to benefit from EGFR-targeted or EGFR pathway-targeted treatments could be identified through immunohistochemistry for EGFR. Not all the EGFR-expressing tumors in our study could be propagated as PDTOs in EGF-containing medium, therefore research to identify additional biomarkers of EGF-dependence is needed.

The EGF-dependence of some pulmonary NET PDTOs raises a broader question: are NETs generally growth-factor dependent? We hypothesize that the identification of additional NET growth-factor dependencies could enable the generation of PDTOs from additional NET subtypes, such as SINETs, which we were not able to propagate long-term in this study. Consistent with this idea, a mouse xenograft study suggests that some pancreatic NETs are dependent on the growth factor, HGF.[77] Beyond model generation, the identification of growth-factor dependencies for NETs could point to new therapeutic strategies aimed at targeting growth-factor mediated pathways in specific patient populations.

Our comprehensive analysis of the genomic features of NEN PDTOs highlights both the fidelity and utility of these models for research on intra-tumoral heterogeneity and tumor evolution. PDTOs not only retain most of the intra-tumoral heterogeneity of their parental tumors, but they also recapitulate the evolutionary forces at work and subclonal dynamics. Our experiments spanned more than a year, and we found that the late passage G3 PDTOs show changes in subclonal composition, while low-grade tumors show no such turnover (e.g., passage 2 of SINET8). The supra-carcinoid PDTO showed a turnover speed similar to that of LCNEC, in line with other evidence suggesting a more aggressive disease.[5] These data argue that PDTOs can be harnessed to study subclonal tumor cell dynamics and tumor evolution. This is critical to accurately model disease treatment resistance and relapse, which is often driven by either pre-existing, low-frequency subclones or novel subclones appearing after the onset of therapy.[78]

Despite our low sample size, our molecular analyses of NEN PDTOs and their parental tumors shed light on NET biology. We saw that evolutionary trajectories can strongly vary across LNETs of different grades and molecular groups. Low-grade tumors such as LNET6 can initiate with a single driver alteration (e.g., a *PSIP1* structural variant[34]) and slowly accumulate neutral (non-driver) alterations due to weak age-related endogenous mutational processes. At the other end of the spectrum, supra-carcinoids like LNET10 can evolve following catastrophic chromosomal events such as chromothripsis, involving multiple cancer genes and fueled by more diverse mutational processes spanning small variants and large structural rearrangements. This is a textbook example of punctuated evolution, where tumor evolution can be stagnant for a few years before undergoing a "leap" due to a catastrophic event.[79,80] Interestingly, LNET10 seems to experience a subsequent selective sweep and to undergo a fast allelic turnover. A recent case study from the Dutch MEN1 Study Group supports this model of progression via punctuated evolution; a pulmonary NET showing an indolent course for six years unexpectedly progressed to aggressive disease likely driven by an activating mutation in *PIK3CA*.[9] Further studies will be needed to determine whether these observations can be generalized and to what degree they represent how slow growing tumors can unexpectedly become clinically aggressive.

Here, we report case studies in LCNEC and supra-carcinoid PDTOs that highlight their utility in the identification of novel therapeutic strategies and biomarkers of treatment response. Consistent with studies showing that solid tumors with a neuroendocrine phenotype show increased sensitivity to an inhibitor of the NAD salvage pathway, FK866, we found that NEN PDTOs are sensitive to this inhibitor.[81] It is tempting to speculate that the neuroendocrine phenotype, associated with the biosynthesis of hormones and neuropeptides, creates targetable metabolic vulnerabilities.

We also identified high expression of *ASCL1* as a potential biomarker for therapeutic response to BCL2 inhibitors. Although the link between *ASCL1* expression and sensitivity to BCL2 inhibitors has been observed in SCLC, it has not previously been explored in LCNEC. We did not see the same link between *NEUROD1* expression and sensitivity to Aurora kinase inhibition as has been observed for SCLC, arguing that not all SCLC therapies and biomarkers apply to LCNEC, and underscoring the need for more preclinical *in vitro* models of LCNEC for hypothesis testing.

Limitations of the study

While *ASCL1* is associated with pulmonary NENs, its overexpression has been reported in some GEP and prostate NECs and our data show that expression of this neuroendocrine transcription factor may have clinical relevance for both pulmonary and extrapulmonary LCNECs.[25,62,82] The questions that follow are, to what degree are LCNECs from different tissue sites similar and might LCNECs across different tissue sites share therapeutic vulnerabilities and biomarkers of response? The LCNEC PDTO samples in this study are not enough to make such a broad generalization, but our data support the idea, and further research is warranted. The ability to classify LCNECs according to shared gene expression profiles, irrespective of tissue site, could aid in overcoming the fact that LCNEC, when divided according to tissue site, is very rare at each site. Another limitation of the study is that we were only able to test the response to EGFR inhibition of one relevant LNET PDTO line. Studies in additional PDTO lines are warranted.

In conclusion, analysis of the unique media dependencies and drug responses of PDTOs in our biobank, combined with a comprehensive examination of their genomic features provide insights into the biology of NENs. We identified potentially actionable vulnerabilities for both low-grade and high-grade disease, highlighting the importance of preclinical models for the entire spectrum of NEN malignancy. Our pulmonary NET PDTOs represent an important resource for the study of this disease and enable studies aimed at identifying mechanisms of disease progression and factors predictive of this progression.

STAR★METHODS

Detailed methods are provided in the online version of this paper and include the following:

- KEY RESOURCES TABLE
- RESOURCE AVAILABILITY

- Lead contact
- Materials availability
- Data and code availability

- EXPERIMENTAL MODELS AND STUDY PARTICIPANT DETAILS
  - Approval of studies involving human and patient-informed consent
  - NEN tissue processing
  - Tumor organoid culture
  - PDTO models
  - Mice
- METHOD DETAILS
  - Xenotransplantation of tumor organoids
  - Histological analyses
  - Tissue microarray analysis
  - RNA and DNA isolation
  - Classification of NEN PDTOs as "high-purity" or "mixed"
  - Nicotinamide assays
  - Quantitation of EGF dependency in lung NET organoids
  - Drug sensitivity tests
  - Whole-genome sequencing
  - RNA sequencing
  - Somatic alteration calling
  - Mutational signatures
  - Evolutionary analyses
- QUANTIFICATION AND STATISTICAL ANALYSES

SUPPLEMENTAL INFORMATION

Supplemental information can be found online at https://doi.org/10.1016/j.ccell.2023.11.007.

ACKNOWLEDGMENTS

We thank all patients participating in this study as well as the teams approaching patients for consent and collecting tissue, including the Utrecht Portal for Organoid Technology (U-PORT; UMC Utrecht)—in particular Anneta Brousali, Jorieke Salij, Onno Kranenburg, and Renate Bezemer—and the clinical studies department at the NKI—in particular Jan-Nico Ridderbos. We are grateful to the Foundation Hubrecht Organoid Technology (HUB) and employees, including Patrick de Kort and Calinda Dingenouts, for their work supporting ethical regulatory affairs. We thank Utrecht Sequencing for bulk RNA sequencing services. We thank the editor and two anonymous reviewers for their comments and suggestions. We acknowledge financial support from the NET Research Foundation (2017 Petersen Accelerator Award to H.C.), Worldwide Cancer Research (2020 grant round to L.F.-C), NET Research Foundation (2019 Investigator Award to L.F.-C), French National Cancer Institute (INCa, PRT-K 2017 to L.F.-C. and M.F.), Ligue Nationale contre le Cancer (fellowship to L.Ma.), and the Dutch Cancer Foundation (grant number 10956, 2017, to E.J.S.). T.L.D. was supported by an EMBO long-term fellowship (ALTF-21-2017) and a Marie Skłodowska-Curie IF grant 797966 – PNECtumor. A.D. was supported by Accelerate Lung Regeneration Consortium grant BREATH 12.0.18.002 of the Lung Foundation Netherlands (to H.C.). The Oncode Institute is supported by the Dutch Cancer Society.

The results shown here are in part based upon data generated by the Rare Cancers Genomics initiative (www.rarecancersgenomics.com) and the TCGA Research Network (https://www.cancer.gov/tcga).

We thank E. Reckzeh and Y.M. Soto-Feliciano for critically reading the manuscript and R. Millen for assistance with drug sensitivity assays.

AUTHOR CONTRIBUTIONS

T.L.D., N.A., L.F.-C., and H.C. designed and conceived the study. T.L.D. generated the organoids. T.L.D., L.dH., and V.G. cultured and curated organoid lines and performed related experiments. T.L.D., V.G., and A.F.M.D. performed drug sensitivity assays. V.G. and J.V. performed xenotransplantation experiments. J.B. and J.D. contributed to study design. L.Mo., L.L., W.M.H., and L.B. performed histological stains, acquired images, and performed related analyses. N.A. processed the sequencing data. T.L.D. and N.A. analyzed and interpreted the data and generated figures. J.V. and H.B. embedded organoids and cut slides for immunohistochemistry staining. S.J. generated novel reagents. L.H., L.B., and S.L. performed pathological assessments. N.A., C.V., and A.vH. curated sequencing data. L.Ma. contributed to analysis of sequencing data. L.Mo., J.D., S.L., R.S.vL., L.B., and K.S. provided samples, curated patient data, and provided pathology information. N.F.M.K., K.J.H., H.M.K., I.H.M.B.R., A.-M.D., G.V., M.R.V., W.B., J.vdB., and M.T. provided clinical feedback. J.D., M.R.V., G.D.V., J.vdB., and M.T. coordinated clinical aspects of the study. L.F.-C. and M.F. supervised N.A., L.Ma., C.V., and A.S.-O. E.-J.S. and J.D. supervised L.Mo. and L.L. H.C. directed the study.

DECLARATION OF INTERESTS

Where authors are identified as personnel of the International Agency for Research on Cancer/World Health Organization, the authors alone are responsible for the views expressed in this article and they do not necessarily represent the decisions, policy or views of the International Agency for Research on Cancer/World Health Organization.

H.C.'s full disclosure is given at https://www.uu.nl/staff/JCClevers/. H.C. is inventor of several patents related to organoid technology, cofounder of Xilis Inc. and currently an employee of Roche, Basel.

INCLUSION AND DIVERSITY

We support inclusive, diverse, and equitable conduct of research.

Received: August 11, 2022
Revised: September 6, 2023
Accepted: November 8, 2023
Published: December 11, 2023

REFERENCES

1. Rindi, G., Mete, O., Uccella, S., Basturk, O., La Rosa, S., Brosens, L.A.A., Ezzat, S., de Herder, W.W., Klimstra, D.S., Papotti, M., and Asa, S.L. (2022). Overview of the 2022 WHO Classification of Neuroendocrine Neoplasms. Endocr. Pathol. *33*, 115–154.
2. Derks, J.L., van Suylen, R.J., Thunnissen, E., den Bakker, M.A., Groen, H.J., Smit, E.F., Damhuis, R.A., van den Broek, E.C., Speel, E.-J.M., and Dingemans, A.-M.C.; PALGA group (2017). Chemotherapy for pulmonary large cell neuroendocrine carcinomas: does the regimen matter? Eur. Respir. J. *49*, 1601838.
3. Korse, C.M., Taal, B.G., van Velthuysen, M.-L.F., and Visser, O. (2013). Incidence and survival of neuroendocrine tumours in the Netherlands according to histological grade: experience of two decades of cancer registry. Eur. J. Cancer *49*, 1975–1983.
4. Baudin, E., Caplin, M., Garcia-Carbonero, R., Fazio, N., Ferolla, P., Filosso, P.L., Frilling, A., de Herder, W.W., Hörsch, D., Knigge, U., et al. (2021). Lung and thymic carcinoids: ESMO Clinical Practice Guidelines for diagnosis, treatment and follow-up. Ann. Oncol. *32*, 439–451.
5. Alcala, N., Leblay, N., Gabriel, A.A.G., Mangiante, L., Hervas, D., Giffon, T., Sertier, A.S., Ferrari, A., Derks, J., Ghantous, A., et al. (2019). Integrative and comparative genomic analyses identify clinically relevant pulmonary carcinoid groups and unveil the supra-carcinoids. Nat. Commun. *10*, 3407.
6. Laddha, S.V., da Silva, E.M., Robzyk, K., Untch, B.R., Ke, H., Rekhtman, N., Poirier, J.T., Travis, W.D., Tang, L.H., and Chan, C.S. (2019). Integrative Genomic Characterization Identifies Molecular Subtypes of Lung Carcinoids. Cancer Res. *79*, 4339–4347.

7. Rekhtman, N., Pietanza, M.C., Hellmann, M.D., Naidoo, J., Arora, A., Won, H., Halpenny, D.F., Wang, H., Tian, S.K., Litvak, A.M., et al. (2016). Next-generation sequencing of pulmonary large cell neuroendocrine carcinoma reveals small cell carcinoma–like and non–small cell carcinoma–like subsets. Clin. Cancer Res. *22*, 3618–3629.

8. Simbolo, M., Barbi, S., Fassan, M., Mafficini, A., Ali, G., Vicentini, C., Sperandio, N., Corbo, V., Rusev, B., Mastracci, L., et al. (2019). Gene Expression Profiling of Lung Atypical Carcinoids and Large Cell Neuroendocrine Carcinomas Identifies Three Transcriptomic Subtypes with Specific Genomic Alterations. J. Thorac. Oncol. *14*, 1651–1661.

9. van den Broek, M.F.M., de Laat, J.M., van Leeuwaarde, R.S., van de Ven, A.C., de Herder, W.W., Dekkers, O.M., Drent, M.L., Kerstens, M.N., Bisschop, P.H., Havekes, B., et al. (2021). The Management of Neuroendocrine Tumors of the Lung in MEN1: Results From the Dutch MEN1 Study Group. J. Clin. Endocrinol. Metab. *106*, e1014–e1027.

10. Hermans, B.C.M., Derks, J.L., Moonen, L., Habraken, C.H.J., der Thüsen, J.v., Hillen, L.M., Speel, E.J.M., and Dingemans, A.-M.C. (2020). Pulmonary neuroendocrine neoplasms with well differentiated morphology and high proliferative activity: illustrated by a case series and review of the literature. Lung Cancer *150*, 152–158.

11. Baine, M.K., and Rekhtman, N. (2020). Multiple faces of pulmonary large cell neuroendocrine carcinoma: update with a focus on practical approach to diagnosis. Transl. Lung Cancer Res. *9*, 860–878.

12. Corbett, V., Arnold, S., Anthony, L., and Chauhan, A. (2021). Management of Large Cell Neuroendocrine Carcinoma. Front. Oncol. *11*, 653162.

13. Andersson-Rolf, A., Clevers, H., and Dayton, T.L. (2021). Diffuse Hormonal Systems. In Endotext, K.R. Feingold, B. Anawalt, A. Boyce, G. Chrousos, W.W. de Herder, K. Dhatariya, K. Dungan, J.M. Hershman, J. Hofland, and S. Kalra, et al., eds. (MDText.com, Inc).

14. Kawasaki, K., Fujii, M., and Sato, T. (2018). Gastroenteropancreatic neuroendocrine neoplasms: genes, therapies and models. Dis. Model. Mech. *11*, dmm029595.

15. Lorz, C., Oteo, M., and Santos, M. (2020). Neuroendocrine Lung Cancer Mouse Models: An Overview. Cancers *13*, 14.

16. Asiedu, M.K., Thomas, C.F., Jr., Tomaszek, S.C., Peikert, T., Sanyal, B., Sutor, S.L., Aubry, M.-C., Li, P., and Wigle, D.A. (2014). Generation and sequencing of pulmonary carcinoid tumor cell lines. J. Thorac. Oncol. *9*, 1763–1771.

17. Gazdar, A.F., Bunn, P.A., and Minna, J.D. (2017). Small-cell lung cancer: what we know, what we need to know and the path forward. Nat. Rev. Cancer *17*, 725–737.

18. Griger, J., Widholz, S.A., Jesinghaus, M., de Andrade Krätzig, N., Lange, S., Engleitner, T., Montero, J.J., Zhigalova, E., Öllinger, R., Suresh, V., et al. (2023). An integrated cellular and molecular model of gastric neuroendocrine cancer evolution highlights therapeutic targets. Cancer Cell *41*, 1327–1344.e10.

19. Sato, T., Stange, D.E., Ferrante, M., Vries, R.G.J., Van Es, J.H., Van den Brink, S., Van Houdt, W.J., Pronk, A., Van Gorp, J., Siersema, P.D., and Clevers, H. (2011). Long-term expansion of epithelial organoids from human colon, adenoma, adenocarcinoma, and Barrett's epithelium. Gastroenterology *141*, 1762–1772.

20. van de Wetering, M., Francies, H.E., Francis, J.M., Bounova, G., Iorio, F., Pronk, A., van Houdt, W., van Gorp, J., Taylor-Weiner, A., Kester, L., et al. (2015). Prospective derivation of a living organoid biobank of colorectal cancer patients. Cell *161*, 933–945.

21. Sachs, N., de Ligt, J., Kopper, O., Gogola, E., Bounova, G., Weeber, F., Balgobind, A.V., Wind, K., Gracanin, A., Begthel, H., et al. (2018). A Living Biobank of Breast Cancer Organoids Captures Disease Heterogeneity. Cell *172*, 373–386.e10.

22. Sachs, N., and Clevers, H. (2014). Organoid cultures for the analysis of cancer phenotypes. Curr. Opin. Genet. Dev. *24*, 68–73.

23. Kim, M., Mun, H., Sung, C.O., Cho, E.J., Jeon, H.-J., Chun, S.-M., Jung, D.J., Shin, T.H., Jeong, G.S., Kim, D.K., et al. (2019). Patient-derived lung cancer organoids as in vitro cancer models for therapeutic screening. Nat. Commun. *10*, 3991.

24. Sachs, N., Papaspyropoulos, A., Zomer-van Ommen, D.D., Heo, I., Böttinger, L., Klay, D., Weeber, F., Huelsz-Prince, G., Iakobachvili, N., Amatngalim, G.D., et al. (2019). Long-term expanding human airway organoids for disease modeling. EMBO J. *38*, e100300.

25. Kawasaki, K., Toshimitsu, K., Matano, M., Fujita, M., Fujii, M., Togasaki, K., Ebisudani, T., Shimokawa, M., Takano, A., Takahashi, S., et al. (2020). An Organoid Biobank of Neuroendocrine Neoplasms Enables Genotype-Phenotype Mapping. Cell *183*, 1420–1435.e21.

26. Dijkstra, K.K., van den Berg, J.G., Weeber, F., van de Haar, J., Velds, A., Kaing, S., Peters, D.D.G.C., Eskens, F.A.L.M., de Groot, D.-J.A., Tesselaar, M.E.T., and Voest, E.E. (2021). Patient-Derived Organoid Models of Human Neuroendocrine Carcinoma. Front. Endocrinol. *12*, 627819.

27. Ebisudani, T., Hamamoto, J., Togasaki, K., Mitsuishi, A., Sugihara, K., Shinozaki, T., Fukushima, T., Kawasaki, K., Seino, T., Oda, M., et al. (2023). Genotype-phenotype mapping of a patient-derived lung cancer organoid biobank identifies NKX2-1-defined Wnt dependency in lung adenocarcinoma. Cell Rep. *42*, 112212.

28. Alvarez, M.J., Subramaniam, P.S., Tang, L.H., Grunn, A., Aburi, M., Rieckhof, G., Komissarova, E.V., Hagan, E.A., Bodei, L., Clemons, P.A., et al. (2018). A precision oncology approach to the pharmacological targeting of mechanistic dependencies in neuroendocrine tumors. Nat. Genet. *50*, 979–989.

29. Hofving, T., Liang, F., Karlsson, J., Yrlid, U., Nilsson, J.A., Nilsson, O., and Nilsson, L.M. (2021). The Microenvironment of Small Intestinal Neuroendocrine Tumours Contains Lymphocytes Capable of Recognition and Activation after Expansion. Cancers *13*, 4305.

30. Gabriel, A.A.G., Mathian, E., Mangiante, L., Voegele, C., Cahais, V., Ghantous, A., McKay, J.D., Alcala, N., Fernandez-Cuesta, L., and Foll, M. (2020). A molecular map of lung neuroendocrine neoplasms. GigaScience *9*, giaa112.

31. Moonen, L., Derks, J., Dingemans, A.M., and Speel, E.J. (2019). Orthopedia Homeobox (OTP) in Pulmonary Neuroendocrine Tumors: The Diagnostic Value and Possible Molecular Interactions. Cancers *11*, 1508.

32. Moonen, L., Mangiante, L., Leunissen, D.J.G., Lap, L.M.V., Gabriel, A., Hillen, L.M., Roemen, G.M., Koch, A., van Engeland, M., Dingemans, A.-M.C., et al. (2022). Differential Orthopedia Homeobox expression in pulmonary carcinoids is associated with changes in DNA methylation. Int. J. Cancer *150*, 1987–1997.

33. Lee, S.H., Hu, W., Matulay, J.T., Silva, M.V., Owczarek, T.B., Kim, K., Chua, C.W., Barlow, L.J., Kandoth, C., Williams, A.B., et al. (2018). Tumor Evolution and Drug Response in Patient-Derived Organoid Models of Bladder Cancer. Cell *173*, 515–528.e17.

34. Fernandez-Cuesta, L., Peifer, M., Lu, X., Sun, R., Ozretić, L., Seidal, D., Zander, T., Leenders, F., George, J., Müller, C., et al. (2014). Frequent mutations in chromatin-remodelling genes in pulmonary carcinoids. Nat. Commun. *5*, 3518.

35. van Riet, J., van de Werken, H.J.G., Cuppen, E., Eskens, F.A.L.M., Tesselaar, M., van Veenendaal, L.M., Klümpen, H.J., Dercksen, M.W., Valk, G.D., Lolkema, M.P., et al. (2021). The genomic landscape of 85 advanced neuroendocrine neoplasms reveals subtype-heterogeneity and potential therapeutic targets. Nat. Commun. *12*, 4612.

36. George, J., Walter, V., Peifer, M., Alexandrov, L.B., Seidel, D., Leenders, F., Maas, L., Müller, C., Dahmen, I., Delhomme, T.M., et al. (2018). Integrative genomic profiling of large-cell neuroendocrine carcinomas reveals distinct subtypes of high-grade neuroendocrine lung tumors. Nat. Commun. *9*, 1048.

37. Cros, J., Théou-Anton, N., Gounant, V., Nicolle, R., Reyes, C., Humez, S., Hescot, S., Thomas de Montpréville, V., Guyétant, S., Scoazec, J.-Y., et al. (2021). Specific Genomic Alterations in High-Grade Pulmonary Neuroendocrine Tumours with Carcinoid Morphology. Neuroendocrinology *111*, 158–169.

38. Derks, J.L., Leblay, N., Lantuejoul, S., Dingemans, A.-M.C., Speel, E.-J.M., and Fernandez-Cuesta, L. (2018). New Insights into the Molecular Characteristics of Pulmonary Carcinoids and Large Cell Neuroendocrine Carcinomas, and the Impact on Their Clinical Management. J. Thorac. Oncol. *13*, 752–766.

39. Miyoshi, T., Umemura, S., Matsumura, Y., Mimaki, S., Tada, S., Makinoshima, H., Ishii, G., Udagawa, H., Matsumoto, S., Yoh, K., et al. (2017). Genomic Profiling of Large-Cell Neuroendocrine Carcinoma of the Lung. Clin. Cancer Res. *23*, 757–765.

40. Pelosi, G., Bianchi, F., Dama, E., Simbolo, M., Mafficini, A., Sonzogni, A., Pilotto, S., Harari, S., Papotti, M., Volante, M., et al. (2018). Most high-grade neuroendocrine tumours of the lung are likely to secondarily develop from pre-existing carcinoids: innovative findings skipping the current pathogenesis paradigm. Virchows Arch. *472*, 567–577.

41. Simbolo, M., Mafficini, A., Sikora, K.O., Fassan, M., Barbi, S., Corbo, V., Mastracci, L., Rusev, B., Grillo, F., Vicentini, C., et al. (2017). Lung neuroendocrine tumours: deep sequencing of the four World Health Organization histotypes reveals chromatin-remodelling genes as major players and a prognostic role for TERT, RB1, MEN1 and KMT2D. J. Pathol. *241*, 488–500.

42. Samsom, K.G., van Veenendaal, L.M., Valk, G.D., Vriens, M.R., Tesselaar, M.E.T., and van den Berg, J.G. (2019). Molecular prognostic factors in small-intestinal neuroendocrine tumours. Endocr. Connect. *8*, 906–922.

43. Zhang, Z., Mäkinen, N., Kasai, Y., Kim, G.E., Diosdado, B., Nakakura, E., and Meyerson, M. (2020). Patterns of chromosome 18 loss of heterozygosity in multifocal ileal neuroendocrine tumors. Genes Chromosomes Cancer *59*, 535–539.

44. Caravagna, G., Sanguinetti, G., Graham, T.A., and Sottoriva, A. (2020). The MOBSTER R package for tumour subclonal deconvolution from bulk DNA whole-genome sequencing data. BMC Bioinf. *21*, 531.

45. Rubanova, Y., Shi, R., Harrigan, C.F., Li, R., Wintersinger, J., Sahin, N., Deshwar, A.G.; PCAWG Evolution and Heterogeneity Working Group, and Morris, Q.D.; PCAWG Consortium (2020). Reconstructing evolutionary trajectories of mutation signature activities in cancer using TrackSig. Nat. Commun. *11*, 731.

46. Vlachogiannis, G., Hedayat, S., Vatsiou, A., Jamin, Y., Fernández-Mateos, J., Khan, K., Lampis, A., Eason, K., Huntingford, I., Burke, R., et al. (2018). Patient-derived organoids model treatment response of metastatic gastrointestinal cancers. Science *359*, 920–926.

47. Tiriac, H., Belleau, P., Engle, D.D., Plenker, D., Deschênes, A., Somerville, T.D.D., Froeling, F.E.M., Burkhart, R.A., Denroche, R.E., Jang, G.-H., et al. (2018). Organoid Profiling Identifies Common Responders to Chemotherapy in Pancreatic Cancer. Cancer Discov. *8*, 1112–1129.

48. Ooft, S.N., Weeber, F., Dijkstra, K.K., McLean, C.M., Kaing, S., van Werkhoven, E., Schipper, L., Hoes, L., Vis, D.J., van de Haar, J., et al. (2019). Patient-derived organoids can predict response to chemotherapy in metastatic colorectal cancer patients. Sci. Transl. Med. *11*, eaay2574.

49. Pasch, C.A., Favreau, P.F., Yueh, A.E., Babiarz, C.P., Gillette, A.A., Sharick, J.T., Karim, M.R., Nickel, K.P., DeZeeuw, A.K., Sprackling, C.M., et al. (2019). Patient-Derived Cancer Organoid Cultures to Predict Sensitivity to Chemotherapy and Radiation. Clin. Cancer Res. *25*, 5376–5387.

50. Yao, Y., Xu, X., Yang, L., Zhu, J., Wan, J., Shen, L., Xia, F., Fu, G., Deng, Y., Pan, M., et al. (2020). Patient-Derived Organoids Predict Chemoradiation Responses of Locally Advanced Rectal Cancer. Cell Stem Cell *26*, 17–26.e6.

51. Christopoulos, P., Engel-Riedel, W., Grohé, C., Kropf-Sanchen, C., von Pawel, J., Gütz, S., Kollmeier, J., Eberhardt, W., Ukena, D., Baum, V., et al. (2017). Everolimus with paclitaxel and carboplatin as first-line treatment for metastatic large-cell neuroendocrine lung carcinoma: a multicenter phase II trial. Ann. Oncol. *28*, 1898–1902.

52. Subbiah, V., Baik, C., and Kirkwood, J.M. (2020). Clinical Development of BRAF plus MEK Inhibitor Combinations. Trends Cancer *6*, 797–810.

53. Yaeger, R., and Corcoran, R.B. (2019). Targeting Alterations in the RAF-MEK Pathway. Cancer Discov. *9*, 329–341.

54. Rindi, G., Klimstra, D.S., Abedi-Ardekani, B., Asa, S.L., Bosman, F.T., Brambilla, E., Busam, K.J., de Krijger, R.R., Dietel, M., El-Naggar, A.K., et al. (2018). A common classification framework for neuroendocrine neoplasms: an International Agency for Research on Cancer (IARC) and World Health Organization (WHO) expert consensus proposal. Mod. Pathol. *31*, 1770–1786.

55. Rudin, C.M., Poirier, J.T., Byers, L.A., Dive, C., Dowlati, A., George, J., Heymach, J.V., Johnson, J.E., Lehman, J.M., MacPherson, D., et al. (2019). Molecular subtypes of small cell lung cancer: a synthesis of human and mouse model data. Nat. Rev. Cancer *19*, 289–297.

56. Gay, C.M., Stewart, C.A., Park, E.M., Diao, L., Groves, S.M., Heeke, S., Nabet, B.Y., Fujimoto, J., Solis, L.M., Lu, W., et al. (2021). Patterns of transcription factor programs and immune pathway activation define four major subtypes of SCLC with distinct therapeutic vulnerabilities. Cancer Cell *39*, 346–360.e7.

57. Lantuejoul, S., Fernandez-Cuesta, L., Damiola, F., Girard, N., and McLeer, A. (2020). New molecular classification of large cell neuroendocrine carcinoma and small cell lung carcinoma with potential therapeutic impacts. Transl. Lung Cancer Res. *9*, 2233–2244.

58. Poirier, J.T., George, J., Owonikoko, T.K., Berns, A., Brambilla, E., Byers, L.A., Carbone, D., Chen, H.J., Christensen, C.L., Dive, C., et al. (2020). New Approaches to SCLC Therapy: From the Laboratory to the Clinic. J. Thorac. Oncol. *15*, 520–540.

59. Mollaoglu, G., Guthrie, M.R., Böhm, S., Brägelmann, J., Can, I., Ballieu, P.M., Marx, A., George, J., Heinen, C., Chalishazar, M.D., et al. (2017). MYC Drives Progression of Small Cell Lung Cancer to a Variant Neuroendocrine Subtype with Vulnerability to Aurora Kinase Inhibition. Cancer Cell *31*, 270–285.

60. Cardnell, R.J., Li, L., Sen, T., Bara, R., Tong, P., Fujimoto, J., Ireland, A.S., Guthrie, M.R., Bheddah, S., Banerjee, U., et al. (2017). Protein expression of TTF1 and cMYC define distinct molecular subgroups of small cell lung cancer with unique vulnerabilities to aurora kinase inhibition, DLL3 targeting, and other targeted therapies. Oncotarget *8*, 73419–73432.

61. Hermans, B.C.M., Derks, J.L., Thunnissen, E., van Suylen, R.J., den Bakker, M.A., Groen, H.J.M., Smit, E.F., Damhuis, R.A., van den Broek, E.C., et al.; PALGA-group (2019). DLL3 expression in large cell neuroendocrine carcinoma (LCNEC) and association with molecular subtypes and neuroendocrine profile. Lung Cancer *138*, 102–108.

62. Yachida, S., Totoki, Y., Noë, M., Nakatani, Y., Horie, M., Kawasaki, K., Nakamura, H., Saito-Adachi, M., Suzuki, M., Takai, E., et al. (2022). Comprehensive Genomic Profiling of Neuroendocrine Carcinomas of the Gastrointestinal System. Cancer Discov. *12*, 692–711.

63. Shida, T., Furuya, M., Kishimoto, T., Nikaido, T., Tanizawa, T., Koda, K., Oda, K., Takano, S., Kimura, F., Shimizu, H., et al. (2008). The expression of NeuroD and mASH1 in the gastroenteropancreatic neuroendocrine tumors. Mod. Pathol. *21*, 1363–1370.

64. Huch, M., Dorrell, C., Boj, S.F., van Es, J.H., Li, V.S.W., van de Wetering, M., Sato, T., Hamer, K., Sasaki, N., Finegold, M.J., et al. (2013). In vitro expansion of single Lgr5+ liver stem cells induced by Wnt-driven regeneration. Nature *494*, 247–250.

65. Verdin, E. (2015). NAD^+ in aging, metabolism, and neurodegeneration. Science *350*, 1208–1213.

66. Holen, K., Saltz, L.B., Hollywood, E., Burk, K., and Hanauske, A.-R. (2008). The pharmacokinetics, toxicities, and biologic effects of FK866, a nicotinamide adenine dinucleotide biosynthesis inhibitor. Invest. New Drugs *26*, 45–51.

67. Galli, U., Colombo, G., Travelli, C., Tron, G.C., Genazzani, A.A., and Grolla, A.A. (2020). Recent Advances in NAMPT Inhibitors: A Novel Immunotherapic Strategy. Front. Pharmacol. *11*, 656.

68. Driehuis, E., Spelier, S., Beltrán Hernández, I., de Bree, R., M Willems, S., Clevers, H., and Oliveira, S. (2019). Patient-Derived Head and Neck Cancer Organoids Recapitulate EGFR Expression Levels of Respective

Tissues and Are Responsive to EGFR-Targeted Photodynamic Therapy. J. Clin. Med. *8*, 1880.

69. Prahallad, A., Sun, C., Huang, S., Di Nicolantonio, F., Salazar, R., Zecchin, D., Beijersbergen, R.L., Bardelli, A., and Bernards, R. (2012). Unresponsiveness of colon cancer to BRAF(V600E) inhibition through feedback activation of EGFR. Nature *483*, 100–103.
70. Capdevila, J., Arqués, O., Hernández Mora, J.R., Matito, J., Caratù, G., Mancuso, F.M., Landolfi, S., Barriuso, J., Jimenez-Fonseca, P., Lopez Lopez, C., et al. (2020). Epigenetic EGFR Gene Repression Confers Sensitivity to Therapeutic BRAFV600E Blockade in Colon Neuroendocrine Carcinomas. Clin. Cancer Res. *26*, 902–909.
71. Driehuis, E., van Hoeck, A., Moore, K., Kolders, S., Francies, H.E., Gulersonmez, M.C., Stigter, E.C.A., Burgering, B., Geurts, V., Gracanin, A., et al. (2019). Pancreatic cancer organoids recapitulate disease and allow personalized drug screening. Proc. Natl. Acad. Sci. USA *116*, 26580–26590.
72. Roerink, S.F., Sasaki, N., Lee-Six, H., Young, M.D., Alexandrov, L.B., Behjati, S., Mitchell, T.J., Grossmann, S., Lightfoot, H., Egan, D.A., et al. (2018). Intra-tumour diversification in colorectal cancer at the single-cell level. Nature *556*, 457–462.
73. Rusch, V.W., Klimstra, D.S., and Venkatraman, E.S. (1996). Molecular markers help characterize neuroendocrine lung tumors. Ann. Thorac. Surg. *62*, 798–809. discussion 809–810.
74. Rickman, O.B., Vohra, P.K., Sanyal, B., Vrana, J.A., Aubry, M.-C., Wigle, D.A., and Thomas, C.F., Jr. (2009). Analysis of ErbB receptors in pulmonary carcinoid tumors. Clin. Cancer Res. *15*, 3315–3324.
75. Bago-Horvath, Z., Sieghart, W., Grusch, M., Lackner, A., Hayden, H., Pirker, C., Komina, O., Węsierska-Gądek, J., Haitel, A., Filipits, M., et al. (2012). Synergistic effects of erlotinib and everolimus on bronchial carcinoids and large-cell neuroendocrine carcinomas with activated EGFR/AKT/mTOR pathway. Neuroendocrinology *96*, 228–237.
76. Bischoff, P., Trinks, A., Wiederspahn, J., Obermayer, B., Pett, J.P., Jurmeister, P., Elsner, A., Dziodzio, T., Rückert, J.C., Neudecker, J., et al. (2022). The single-cell transcriptional landscape of lung carcinoid tumors. Int. J. Cancer *150*, 2058–2071.
77. Krampitz, G.W., George, B.M., Willingham, S.B., Volkmer, J.-P., Weiskopf, K., Jahchan, N., Newman, A.M., Sahoo, D., Zemek, A.J., Yanovsky, R.L., et al. (2016). Identification of tumorigenic cells and therapeutic targets in pancreatic neuroendocrine tumors. Proc. Natl. Acad. Sci. USA *113*, 4464–4469.
78. Marusyk, A., Janiszewska, M., and Polyak, K. (2020). Intratumor Heterogeneity: The Rosetta Stone of Therapy Resistance. Cancer Cell *37*, 471–484.
79. Gould, S.J., and Eldredge, N. (1972). Punctuated equilibria: an alternative to phyletic gradualism. In Models in Paleobiology, T.M.J. Schopf, ed. (Freeman, Cooper & Co), pp. 82–115.
80. Vendramin, R., Litchfield, K., and Swanton, C. (2021). Cancer evolution: Darwin and beyond. EMBO J. *40*, e108389.
81. Balanis, N.G., Sheu, K.M., Esedebe, F.N., Patel, S.J., Smith, B.A., Park, J.W., Alhani, S., Gomperts, B.N., Huang, J., Witte, O.N., and Graeber, T.G. (2019). Pan-cancer Convergence to a Small-Cell Neuroendocrine Phenotype that Shares Susceptibilities with Hematological Malignancies. Cancer Cell *36*, 17–34.e7.
82. Cejas, P., Xie, Y., Font-Tello, A., Lim, K., Syamala, S., Qiu, X., Tewari, A.K., Shah, N., Nguyen, H.M., Patel, R.A., et al. (2021). Subtype heterogeneity and epigenetic convergence in neuroendocrine prostate cancer. Nat. Commun. *12*, 5775.
83. George, J., Lim, J.S., Jang, S.J., Cun, Y., Ozretić, L., Kong, G., Leenders, F., Lu, X., Fernández-Cuesta, L., Bosco, G., et al. (2015). Comprehensive genomic profiles of small cell lung cancer. Nature *524*, 47–53.
84. Di Tommaso, P., Chatzou, M., Floden, E.W., Barja, P.P., Palumbo, E., and Notredame, C. (2017). Nextflow enables reproducible computational workflows. Nat. Biotechnol. *35*, 316–319.
85. Vasimuddin, M., Misra, S., Li, H., and Aluru, S. (2019). Efficient Architecture-Aware Acceleration of BWA-MEM for Multicore Systems. In 2019 IEEE International Parallel and Distributed Processing Symposium (IPDPS), pp. 314–324.
86. Dobin, A., Davis, C.A., Schlesinger, F., Drenkow, J., Zaleski, C., Jha, S., Batut, P., Chaisson, M., and Gingeras, T.R. (2013). STAR: ultrafast universal RNA-seq aligner. Bioinformatics *29*, 15–21.
87. Mose, L.E., Perou, C.M., and Parker, J.S. (2019). Improved indel detection in DNA and RNA via realignment with ABRA2. Bioinformatics *35*, 2966–2973.
88. Kim, S., Scheffler, K., Halpern, A.L., Bekritsky, M.A., Noh, E., Källberg, M., Chen, X., Kim, Y., Beyter, D., Krusche, P., and Saunders, C.T. (2018). Strelka2: fast and accurate calling of germline and somatic variants. Nat. Methods *15*, 591–594.
89. Shale, C., Cameron, D.L., Baber, J., Wong, M., Cowley, M.J., Papenfuss, A.T., Cuppen, E., and Priestley, P. (2022). Unscrambling cancer genomes via integrated analysis of structural variation and copy number. Cell Genom *2*, 100112.
90. Islam, S.A., Díaz-Gay, M., Wu, Y., Barnes, M., Vangara, R., Bergstrom, E.N., He, Y., Vella, M., Wang, J., Teague, J.W., et al. (2022). Uncovering novel mutational signatures by de novo extraction with SigProfilerExtractor. Cell Genom. *2*, 100179.
91. Shannon, P., Markiel, A., Ozier, O., Baliga, N.S., Wang, J.T., Ramage, D., Amin, N., Schwikowski, B., and Ideker, T. (2003). Cytoscape: a software environment for integrated models of biomolecular interaction networks. Genome Res. *13*, 2498–2504.
92. Gillis, S., and Roth, A. (2020). PyClone-VI: scalable inference of clonal population structures using whole genome data. BMC Bioinf. *21*, 571.
93. Rohart, F., Gautier, B., Singh, A., and Lê Cao, K.A. (2017). mixOmics: An R package for 'omics feature selection and multiple data integration. PLoS Comput. Biol. *13*, e1005752.
94. Paczkowska, M., Barenboim, J., Sintupisut, N., Fox, N.S., Zhu, H., Abd-Rabbo, D., Mee, M.W., Boutros, P.C., and Reimand, J.; PCAWG Consortium; PCAWG Drivers and Functional Interpretation Working Group (2020). Integrative pathway enrichment analysis of multivariate omics data. Nat. Commun. *11*, 735.
95. Pertea, M., Pertea, G.M., Antonescu, C.M., Chang, T.-C., Mendell, J.T., and Salzberg, S.L. (2015). StringTie enables improved reconstruction of a transcriptome from RNA-seq reads. Nat. Biotechnol. *33*, 290–295.
96. Hoadley, K.A., Yau, C., Hinoue, T., Wolf, D.M., Lazar, A.J., Drill, E., Shen, R., Taylor, A.M., Cherniack, A.D., Thorsson, V., et al. (2018). Cell-of-Origin Patterns Dominate the Molecular Classification of 10,000 Tumors from 33 Types of Cancer. Cell *173*, 291–304.e6.
97. Alcala, N., Voegele, C., Mangiante, L., Sexton-Oates, A., Clevers, H., Fernandez-Cuesta, L., Dayton, T.L., and Foll, M. (2023). Multi-omic dataset of patient-derived tumor organoids of neuroendocrine neoplasms. Preprint at bioRxiv *1*.
98. Koboldt, D.C. (2020). Best practices for variant calling in clinical sequencing. Genome Med. *12*, 91.
99. Wala, J.A., Bandopadhayay, P., Greenwald, N.F., O'Rourke, R., Sharpe, T., Stewart, C., Schumacher, S., Li, Y., Weischenfeldt, J., Yao, X., et al. (2018). SvABA: genome-wide detection of structural variants and indels by local assembly. Genome Res. *28*, 581–591.
100. Rausch, T., Zichner, T., Schlattl, A., Stütz, A.M., Benes, V., and Korbel, J.O. (2012). DELLY: structural variant discovery by integrated paired-end and split-read analysis. Bioinformatics *28*, i333–i339.
101. Chen, X., Schulz-Trieglaff, O., Shaw, R., Barnes, B., Schlesinger, F., Källberg, M., Cox, A.J., Kruglyak, S., and Saunders, C.T. (2016). Manta: rapid detection of structural variants and indels for germline and cancer sequencing applications. Bioinformatics *32*, 1220–1222.
102. Mangiante, L., Alcala, N., Sexton-Oates, A., Di Genova, A., Gonzalez-Perez, A., Khandekar, A., Bergstrom, E.N., Kim, J., Liu, X., Blazquez-Encinas, R., et al. (2023). Multiomic analysis of malignant pleural

mesothelioma identifies molecular axes and specialized tumor profiles driving intertumor heterogeneity. Nat. Genet. *55*, 607–618.

103. Jeffares, D.C., Jolly, C., Hoti, M., Speed, D., Shaw, L., Rallis, C., Balloux, F., Dessimoz, C., Bähler, J., and Sedlazeck, F.J. Transient Structural Variations Have Strong Effects on Quantitative Traits and Reproductive Isolation in Fission Yeast.Nat. Commun. 8:14061.
104. Nilsen, G., Liestøl, K., Van Loo, P., Moen Vollan, H.K., Eide, M.B., Rueda, O.M., Chin, S.-F., Russell, R., Baumbusch, L.O., Caldas, C., et al. (2012). Copynumber: Efficient algorithms for single- and multi-track copy number segmentation. BMC Genom. *13*, 591.
105. Ioannidis, N.M., Rothstein, J.H., Pejaver, V., Middha, S., McDonnell, S.K., Baheti, S., Musolf, A., Li, Q., Holzinger, E., Karyadi, D., et al. (2016). REVEL: An Ensemble Method for Predicting the Pathogenicity of Rare Missense Variants. Am. J. Hum. Genet. *99*, 877–885.
106. Sei, Y., Zhao, X., Forbes, J., Szymczak, S., Li, Q., Trivedi, A., Voellinger, M., Joy, G., Feng, J., Whatley, M., et al. (2015). A Hereditary Form of Small Intestinal Carcinoid Associated With a Germline Mutation in Inositol Polyphosphate Multikinase. Gastroenterology *149*, 67–78.
107. Walter, D., Harter, P.N., Battke, F., Winkelmann, R., Schneider, M., Holzer, K., Koch, C., Bojunga, J., Zeuzem, S., Hansmann, M.L., et al. (2018). Genetic heterogeneity of primary lesion and metastasis in small intestine neuroendocrine tumors. Sci. Rep. *8*, 3811.
108. Banck, M.S., Kanwar, R., Kulkarni, A.A., Boora, G.K., Metge, F., Kipp, B.R., Zhang, L., Thorland, E.C., Minn, K.T., Tentu, R., et al. (2013). The genomic landscape of small intestine neuroendocrine tumors. J. Clin. Invest. *123*, 2502–2508.
109. Simbolo, M., Vicentini, C., Mafficini, A., Fassan, M., Pedron, S., Corbo, V., Mastracci, L., Rusev, B., Pedrazzani, C., Landoni, L., et al. (2018). Mutational and copy number asset of primary sporadic neuroendocrine tumors of the small intestine. Virchows Arch. *473*, 709–717.
110. Mayakonda, A., Lin, D.-C., Assenov, Y., Plass, C., and Koeffler, H.P. (2018). Maftools: efficient and comprehensive analysis of somatic variants in cancer. Genome Res. *28*, 1747–1756.
111. Gu, Z., Gu, L., Eils, R., Schlesner, M., and Brors, B. (2014). circlize Implements and enhances circular visualization in R. Bioinformatics *30*, 2811–2812.
112. Nik-Zainal, S., Van Loo, P., Wedge, D.C., Alexandrov, L.B., Greenman, C.D., Lau, K.W., Raine, K., Jones, D., Marshall, J., Ramakrishna, M., et al. (2012). The life history of 21 breast cancers. Cell *149*, 994–1007.
113. Dang, H.X., White, B.S., Foltz, S.M., Miller, C.A., Luo, J., Fields, R.C., and Maher, C.A. (2017). ClonEvol: clonal ordering and visualization in cancer sequencing. Ann. Oncol. *28*, 3076–3082.
114. Miller, C.A., McMichael, J., Dang, H.X., Maher, C.A., Ding, L., Ley, T.J., Mardis, E.R., and Wilson, R.K. (2016). Visualizing tumor evolution with the fishplot package for R. BMC Genom. *17*, 880.
115. Jost, L. (2008). G(ST) and its relatives do not measure differentiation. Mol. Ecol. *17*, 4015–4026.
116. Jost, L., Archer, F., Flanagan, S., Gaggiotti, O., Hoban, S., and Latch, E. (2018). Differentiation measures for conservation genetics. Evol. Appl. *11*, 1139–1148.
117. Nei, M., and Chesser, R.K. (1983). Estimation of fixation indices and gene diversities. Ann. Hum. Genet. *47*, 253–259.
118. Benjamini, Y., and Hochberg, Y. (1995). Controlling the false discovery rate: A practical and powerful approach to multiple testing. J. R. Stat. Soc. *57*, 289–300.

STAR★METHODS

KEY RESOURCES TABLE

REAGENT or RESOURCE	SOURCE	IDENTIFIER
Antibodies		
Mouse monoclonal anti-Chromogranin A (LK2H10)	Thermo Scientific	MA5-13096
Mouse monoclonal anti-human Ki67 antigen (MIB-1)	Agilent-Dako	GA62661-2; RRID: AB_2687921
Mouse monoclonal anti-human Synaptophysin	Dako	GA660
Mouse monoclonal anti-human NCAM1/CD56 (clone 123C3)	Dako	IR628
Rabbit monoclonal anti-EGFR (EP22)	Cell Marque	CMC41432010
Chemicals, peptides, and recombinant proteins		
DNase I	Sigma-Aldrich	Catalog #DN25
Collagenase	Sigma	C9407
red blood cell lysis buffer	Roche	11814389001
Dispase II	Thermo Fisher	Cat# 17105041
RNALater Stabilization Solution	Thermo Fisher	AM7020
Advanced DMEM/F12	Thermo Fisher scientific	12634–010
DMEM + GlutaMAX		31966–021
B-27 Supplement		17504044
GlutaMAX		35050061
HEPES		15630080
Penicillin-Streptomycin		15140122
Noggin-Fc fusion protein	ImmunoPrecise	Cat# N002
R-spondin1 conditioned medium	made in house	
N-acetyl-L-cysteine	Sigma-Aldrich	A1965
Nicotinamide	Sigma-Aldrich	N0636
Human EGF	Peprotech	AF-100-15
A83-01	Tocris	2939
Prostaglandin E2	Tocris	2296
SB 202190 (p38 inhibitor)	Sigma-Aldrich	S7076
Y-27632 dihydrochloride (ROCK inhibitor)	Abmole	M1817
Primocin	Invivogen	ant-pm-2
Cultrex Basement Membrane Extract (BME), Growth Factor Reduced, Type 2	R&D Systems, Bio-Techne	3533-010-02
Formaldehyde Solution 4%	Sigma-Aldrich	1.00496
TrypLE Express	Thermo Fisher Scientific	12605010
CHIR (Chir99021)	Stemgent	Cat# 04-0004-10
FGF2	Peprotech	Cat# 100-18B
FGF7	Peprotech	Cat# 100-19
FGF10	Peprotech	Cat# 100-26
Staurosporine	Sigma Aldrich	S4400
Paclitaxel	Selleckchem	S1150
Everolimus (RAD001) (1 mL 10 mM in DMSO)	Selleckchem	S1120
Trametinib	MedChem Express	HY-10999
Dabrafenib (1 mL 10 mM in DMSO)	Selleckchem	S2807
Navitoclax (ABT-263) (1 mL 10 mM in DMSO)	Selleckchem	S1001

(*Continued on next page*)

Continued

REAGENT or RESOURCE	SOURCE	IDENTIFIER
Alisertib (MLN8237) (1 mL 10 mM in DMSO)	Selleckchem	S1133
FK-866/Daporinad	Selleckchem	S2799
Allitinib (1 mL 10 mM in DMSO)	Selleckchem	S2185
Afatinib (1 mL 10 mM in DMSO)	Selleckchem	S1011
Critical commercial assays		
RNeasy Mini Kit	QIAGEN	Cat# 74104
All-Prep DNA/RNA Kit	QIAGEN	Cat# 80204
RNase-free DNase Set	QIAGEN	Cat# 79254
CellTiter-Glo 3D Cell Viability Assay	Promega	Cat# G9683
MycoAlert mycoplasma detection kit	Lonza	Cat# LT07-318
Qubit dsDNA HS Assay Kit	Thermo Fisher	Cat# Q32854
EnVision FLEX Visualization kit	Dako	K8002
Deposited data		
LUAD and LUSC cohorts somatic mutations (TCGA)	GDC data portal	LUAD; LUSC
Next-generation sequencing data of lung NENs (RNA-seq)	Alcala et al.[5]	EGA: EGAS00001003699
Next-generation sequencing data of small intestine NETs (RNA-seq)	Alvarez et al.[28]	SRA: SRP107025
Next-generation sequencing data of small intestine NETs (RNA-seq)	Hofving et al.[29]	EGA: EGAS00001003358
Next-generation sequencing data of SCLC (RNA-seq)	George et al.[83]	EGA: EGAS00001000925
Next-generation sequencing data for PDTOs and their matched original tumors (WGS and RNA-seq)	this study	EGA: EGAS00001005752
Experimental models: Cell lines		
NEN patient-derived tumor organoids	this study	Table S1
Pancreatic ductal adenocarcinoma PDTOs	Driehuis et al.[71]	PDO17, PDO23, PDO19
Colorectal Cancer PDTOs	Roerink, Sasaki, Lee-Six et al.[72]	CRC T3-3/P3.T2.1, CRC T3-1/P3.T4.1
Software and algorithms		
Nextflow version 20.10.0.5430	Seqera labs[84]	https://www.nextflow.io/
GATK version 4.1.7.0	Broad institute	https://gatk.broadinstitute.org/hc/en-us
bwa2 version 2.0	Vasimuddin et al.[85]	https://github.com/bwa-mem2/bwa-mem2
Trim-galore version 0.6.5	Babraham Institute	https://www.bioinformatics.babraham.ac.uk/projects/trim_galore
STAR version 2.7.3a	Dobin et al.[86]	
ABRA2 version 2.22	Mose et al.[87]	
StringTie version 2.1.2	Pertea et al.[95]	
Strelka2 version 2.9.10	Kim et al.[88]	
SVaba version 1.1.0	Wala et al.[99]	
Delly version 0.8.7	Rausch et al.[100]	
Manta version 1.6.0	Chen et al.[101]	
SURVIVOR version 1.0.7	Jeffares et al.[103]	
PURPLE version 2.52	Shale et al.[89]	https://github.com/hartwigmedical/hmftools/tree/master/purple
SigProfilerExtractor version 1.1.3	Islam et al.[90]	
Cytoscape version 3.9.1	Shannon et al.[91]	https://cytoscape.org/
Pyclone-VI	Gillis et al.[92]	

(*Continued on next page*)

Continued

REAGENT or RESOURCE	SOURCE	IDENTIFIER
R version 4.1.2	R CRAN	
R package trend version 1.1.4	R CRAN	
R package ggridges version 0.5.3	R CRAN	
R package umap version 0.2.8.0	R CRAN	
R package mixOmics version 6.18.1	Bioconductor[93]	
R package ActivePathways version 1.1.0	R CRAN[94]	
R package maftools version 2.2.10	R CRAN[110]	
R package DPclust version 2.2.8	Github[112]	https://github.com/Wedge-lab/dpclust
R package dpclust3p version 1.0.8	github	https://github.com/Wedge-lab/dpclust3p
R package eulerr version 6.1.1	R CRAN	https://github.com/jolars/eulerr
R package mobster version 1.0.0	Github[44]	
R package circlize version 0.4.13	R CRAN[111]	
R package ggpointdensity version 0.1.0	R CRAN	
R package copynumber version 1.20.0	R CRAN	
R package TrackSig version 0.2.0	Github[45]	https://github.com/morrislab/TrackSigFreq
R package clonevol version 0.99.11	Github[113]	https://github.com/hdng/clonevol
R package fishplot version 0.5.1	Github[114]	https://github.com/chrisamiller/fishplot
Biorender	Biorender	http:/biorender.com (agreement number PO2499GT9Q)
Other		
Agilent2100 Bioanalyzer	Agilent	
Bioanalyzer2100 RNA Nano 6000 chips	Agilent	Cat# 5067-1511
Multi-drop Combi Reagent Dispenser	Thermo Fisher	
D300e Digital Dispenser	Tecan	
Spark multimode microplate reader	Tecan	
Link 48 Autostainer Platform	Dako	
SpinVessel 50 mL conical tubes	V&P Scientific, Inc	VP 830SV-50CB
SpinVessel	V&P Scientific, Inc	VP 418SV2-2-50CB-CC

RESOURCE AVAILABILITY

Lead contact

Further information and requests for resources and reagents should be directed to and will be fulfilled by the Lead Contact, Hans Clevers (h.clevers@hubrecht.eu).

Materials availability

Organoid lines reported in this manuscript can be requested from the lead author, h.clevers@hubrecht.eu and/or from talya.dayton@embl.es. Distribution of organoids to third parties will have to be authorized by the relevant ethical committee and a complete MTA will be required to ensure compliance with the Dutch 'medical research involving human subjects' act. Use of organoids is subjected to patient consent; upon consent withdrawal, distributed organoid lines and any derived material will have to be promptly disposed of.

Data and code availability

The raw and processed next-generation sequencing data generated for this study were deposited on the European Genome-phenome Archive (EGA) (accession code EGA: EGAS00001005752). We also used public RNA-seq datasets available on EGA, for lung NENs (accession code EGA: EGAS00001003699), small intestine NETs (accession code EGA: EGAS00001003358), small cell lung cancer (accession code EGA: EGAS00001000925), and a dataset of small intestine NETs available from the short reads archive (SRA, accession code SRA: SRP107025). We retrieved a public list of somatic mutations in lung adenocarcinoma (LUAD) and squamous cell carcinoma (LUSC) from the TCGA project using the GDC data portal. All bioinformatic processing pipelines are open-source and freely accessible via Github at https://github.com/IARCbioinfo/. Analysis scripts used to analyze the sequencing data and produce the related figures are available via Github at https://github.com/IARCbioinfo/MS_panNEN_organoids.

EXPERIMENTAL MODELS AND STUDY PARTICIPANT DETAILS

Approval of studies involving human and patient-informed consent

The collection of patient data and tissue for the generation and distribution of normal and NEN organoids was performed according to the guidelines of the European Network of Research Ethics Committees (EUREC) following European, national and local law. The protocols were approved by the medical ethical committee (METC) corresponding to the respective hospitals where patients were treated: Verenigde Commissies Mensgebonden Onderzoek of the St. Antonius Hospital Nieuwegein, Z-12.55; UMC Utrecht, METC 12–093 HUB-Cancer; NKI Institutional Review Board (IRB), M18ORG/CFMPB582; Maastricht University Medical Center, METC 2019-1061, and 2019-1039. All patients participating in this study signed informed consent forms and could withdraw their consent at any time.

NEN tissue processing

On arrival, NEN tissues were cut into 3–5 mm^3 pieces. Two or three random pieces were placed in RNAlater solution and stored at −80°C for DNA and RNA isolation, one random piece was fixed in formalin for histopathological analysis and immunohistochemistry, and the remainder were processed for organoid derivation. For organoid derivation: tissue was minced, collected with 10 mL DMEM containing antibiotics, and transferred to a 15 mL conical tube. To dissociate the minced tissue further, 200 μL of collagenase solution (20 mg mL−1) was added to the tissue/DMEM solution and the tube was placed on an orbital shaker at 37°C for 25 min. After digestion, 50 μL of DNase I solution (10 mg/mL) was added. The digested tissue suspension was sheared using 5 mL plastic pipettes, strained over a 100 μm filter. Large tissue pieces that remained after digestion were presumed to be necrotic or fibrotic and discarded. The filtered tissue suspension was centrifuged at 1,000 r.p.m. and the supernatant was removed. In case of a visible red pellet, erythrocytes were lysed in 50–300 μL of red blood cell lysis buffer (depending on pellet size) for 5 min at room temperature and then washed twice with 13 mL DMEM containing antibiotics. Finally, the pellet was resuspended in appropriate volume of BME for plating in 30 μL droplets on preheated suspension plates (Greiner).

Tumor organoid culture

NEN patient-derived tumor organoids were grown in 30 μL drops of BME in suspension culture plates, overlaid with growth medium. The growth medium consisted of Advanced DMEM/F12 supplemented with 1x GlutaMAX, 10 mM HEPES, penicillin-streptomycin, Primocin (InvivoGen, Cat# N001), 1% Noggin conditioned medium (U-Protein Express, Cat# N002), 20% of RSPO3 conditioned medium (made in-house), 1x B27 supplement (GIBCO, Cat# 175044), 1.25 mM n-Acetylcystein (Sigma, Cat# A9165), 3 μM CHIR (Stemgent, Cat# 04-0004-10), 1 μM Prostaglandin E2 (Tocris, Cat# 2296), 0.005 μg/mL FGF2 (Peprotech), 10 μM ROCK inhibitor (Abmole, Cat# Y27632), 500 nM A83-01 (Tocris, Cat# 2939), 3 μM p38 inhibitor SB202190 (Sigma, Cat# 7067). Note that the primary difference of this medium compared to published media is the addition of CHIR and FGF2, with CHIR making a clear difference in supporting organoid growth while FGF2 impact was not entirely clear. All lung NET organoids and some LCNEC organoids were grown in media additionally supplemented with 0.05 μg/mL EGF (Peprotech, Cat# AF-100-15). Media was changed once a week.

For splitting, a 2 min incubation in TrypLE at 37°C was followed by mechanical shearing through a p10 tip attached a fire-polished plugged glass pipettes (Fisher Scientific, Cat# 11506973) was used to break organoids up into small clusters of cells. Following isolation, LCNEC lines were consistently passaged at an approximate splitting ratio of 1:12 every 14 days. Pulmonary NET lines show a high degree of variability in their growth rates and required passaging at a split ratio of 1:2 or 1:3 every 2 months for lines derived from grade 2 tumors and once every 3 months of lines derived from grade 1 tumors. SI NET PDTOs showed a similar growth rate as pulmonary NET PDTOs but could not be passaged more than 4 times. All organoid lines tested negative in the MycoAlert mycoplasma detection kit (Lonza, LT07-318).

PDTO models

All NEN PDTO models were generated as described for this study. Pancreatic Adenocarcinoma PDTO lines, PDO17, PDO19, and PDO23 were generated and reported in a previous study.[71] Colorectal Cancer PDTO lines, CRC T3-3/P3.T2.1 and CRC T3-1/P3.T4.1, were generated and reported in a previous study.[72]

Mice

For PDTO xeno-transplantations, NOD.Cg-Prkdcscid Il2rgtm1Wjl/SzJ (NSG) mice were used. Transplantation experiments were performed after institutional review by the Animal Ethics Committee of the Royal Netherlands Academy of Arts and Sciences (KNAW) with project license of AVD8010020209924 and research protocol HICle9924.22.02.

METHOD DETAILS

Xenotransplantation of tumor organoids

NEN PDTOs were collected for transplantation 7 to 10 days after splitting. On the day of transplantation, organoids were released from the basement membrane extract (BME) and a small portion of the total sample was dissociated into single cells to estimate the cellular density of each sample. Approximately 100 000 cells were suspended in 100 μL of medium mixed with BME at a 1:1 ratio. Subcutaneous injections were performed into opposite flanks of all 3–4 NSG mice per line (2 flanks per mouse, 100 000 cells per location). The mice were sacrificed 73–108 days after injections. Tumor measurements were taken by digital calipers (RS PRO,

Cat# 841–2518) and volumes estimated by formula: tumor volume = (length x width^2)/2, where length represents the largest tumor diameter and width the perpendicular tumor diameter. All tumors were subjected to immunohistochemical analysis.

Histological analyses

Tissue and organoids were fixed overnight in 4% paraformaldehyde and subsequently dehydrated, paraffin embedded, and sectioned. Standard H&E staining was performed and stained sections were blindly analyzed by a pathologist specialized in NENs. WHO 2021 criteria for NENs were applied. Immunohistochemistry was performed using antibodies against Chromogranin A (Thermo Scientific, clone: LK2H10) dilution 1:1000, Ki67 clone MIB-1 (DAKO, 'ready to use'), Synaptophysin (DAKO, 'ready to use'), CD56/NCAM1 (DAKO, 'ready to use'), and EGFR (Cell Marque, EP22, 1:200). All stainings were performed using the DAKO Link 48 Autostainer Platform and the EnVision FLEX Visualization kit (DAKO, cat# K8002) according to standard diagnostic routine protocols and manufacturer instructions. Immunohistochemical stainings were evaluated by pathologists (L. Brosens, or L.M. Hillen and S. Lantuejoul), who were blinded for all clinical, histopathological, and sequencing data. Slides were scanned using a Pannoramic 1000 slide scanner (3DHISTECH Ltd) and images were acquired using the CaseViewer software (3DHISTECH Ltd).

Tissue microarray analysis

EGFR expression in human pulmonary neuroendocrine tumors was analyzed in two tissue microarrays (TMA) from the Maastricht University Medical Center (MUMC+), jointly containing cores derived from 70 tumors. Each tumor on the TMAs was represented by 3 cores derived from both central and peripheral tumor regions. Each TMA core was independently scored for EGFR IHC intensity and membrane localization and given a score of either high, medium, low, or absent EGFR membrane expression, where at least 20% of tumor cells were positive. In the majority of positive cases 70 to 100% of tumor cells were positive. Subsequently, tumors were assigned an overall score. In cases where cores from the same tumor were given a different EGFR IHC score, the tumor was assigned the score consistent between at least 2 out of the 3 cores (see Table S5).

RNA and DNA isolation

RNA was isolated from NEN organoids using the RNeasy Mini Kit (QIAGEN, Cat# 74104) following the manufacturer's instructions including DNaseI treatment (QIAGEN, Cat# 79254). RNA and DNA were isolated from the same sample of NEN organoids and/or tissue using the All Prep DNA/RNA Mini Kit (QIAGEN, Cat # 80204) following the manufacturer's instructions.

Classification of NEN PDTOs as "high-purity" or "mixed"

Established NEN PDTO lines were classified as either "high-purity" or "mixed" according to available data derived from: morphological/histological analyses and molecular analyses. The term "high-purity" was applied to PDTO lines for which there was no discernible contamination in the organoids from non-tumor cells as identified by either histology or molecular analyses. The term "mixed" was applied to PDTOs for which histology and/or molecular analyses provided evidence for the presence of both tumor cells and non-tumor cells. The following criteria were defined as evidence of tumor cells in the culture: 1) presence of neuroendocrine marker-expressing cells identified by immunohistochemical staining (CHGA, SYP, or CD56/NCAM); 2) levels of neuroendocrine marker expression within the range observed for corresponding subtype in reference dataset (Figures 3 and S3; Table S2); 3) UMAP clustering of organoid sample together with corresponding parental tumor tissue (Figures 3 and S3); 4) identification of shared genetic driver or NEN-associated alterations in PDTO and parental tumors by WGS (when available); 5) identification of genetic driver or NEN-associated alterations in RNAseq reads (applied when WGS data were not available) (Figures 4 and S4; Table S4).

In all cases, a sample was defined as "pure" by criteria 1 when 60% or more of cells were NE-marker positive, and "mixed" when less than 60% of cells were NE-marker positive. For lines that were defined as "mixed" by criteria 1, evidence of tumor cell content by criterias 2–5 were used to determine whether the NE-marker+ cells were likely to be tumor cells (i.e., criteria 2–5 were used to classify lines for which criteria 1 showed less than 60% of cells were NE-marker+). When WGS data were available, tumor purity was estimated jointly with the copy number alterations using software PURPLE (see "copy number variant calling" paragraph below). One sample, LNET2Np7, derived from tumor adjacent normal tissue of LNET2 patient was assessed using this criteria. However, WGS analyses were inconclusive with regards to tumor cell content. Given the concurrent diagnosis of diffuse idiopathic pulmonary neuroendocrine cell hyperplasia (DIPNECH) in this patient and the high likelihood of DIPNECH cells in the "normal adjacent tissue," this sample was removed from downstream analyses.

Nicotinamide assays

Single cells (4,000) were plated in 5 μL of BME in the wells of a 96 well plate and overlaid with media containing different concentrations of nicotinamide. Following expansion and organoid formation (one to four weeks depending on the line), ATP levels were measured using the CellTiter-Glo 3D Reagent (Promega, catalog no. G9681) according to the manufacturer's instructions, and luminescence was measured using a Spark multimode microplate reader (Tecan). Results for each line were normalized to the value for that line in 10 mM nicotinamide, the standard concentration used in organoid culture (100%).

Quantitation of EGF dependency in lung NET organoids

Single cells (4,000) were plated in 5 μL of BME in the wells of a 96 well plate and overlaid with media containing different concentrations of EGF. Following expansion and organoid formation (one to ten weeks depending on the line), ATP levels were measured using

the CellTiter-Glo 3D Reagent (Promega, catalog no. G9681) according to the manufacturer's instructions, and luminescence was measured using a Spark multimode microplate reader (Tecan). Results for each line were normalized to the value for that line in media lacking EGF (100%). Values shown in the graph were then normalized across rows by dividing by the highest viability value.

Drug sensitivity tests

Prior to the start of the drug screen, TrypLE was used to disrupt organoids into single cells and small clusters of cells that were then plated in 30 μL drops BME in the wells of a 6 well plate. Organoids were then grown in the appropriate media as for regular expansion. Seven to ten days later, organoids were collected from the BME by the addition of 1 mg/mL dispase II (Sigma-Aldrich, catalog no. D4693) to the medium of the organoids. Organoids were incubated for 90 min at 37°C to digest the BME. Following collection of organoids and washing with DMEM to remove dispase, organoids were filtered using a 70-mm nylon cell strainer (BD Falcon), counted, and resuspended in 5% BME/growth medium (12,500 organoids/mL) and transferred to SpinVessel 50 mL conical bottom tubes. The SpinVessel tubes containing the organoid solution were placed on a SpinVessel machine and rotated at speed setting 25 so as to keep organoids in a homogeneous solution. Finally, 40 μL volume of organoid solution was dispensed (Multidrop Combi Reagent Dispenser, Thermo Scientific, catalog no. 5840300) in 384-well plates (Corning, catalog no. 4588).

Drugs were added 3 days after plating using the Tecan D300e Digital Dispenser (Tecan). The time in between plating and addition of drugs was maintained to allow organoids to recover after plating. All drugs in the assays were dissolved in DMSO and all wells were normalized for DMSO percentage, which never exceeded 1%. Drug exposure was performed in triplicate for each concentration shown and drug assays were repeated at least once for all drugs. When available drugs were purchased as 1 mL of a 10 mM solution in DMSO (See reagents table). For FK866 5 mM solution was made in DMSO and further diluted to reach the assay concentrations. 10 mM solutions in DMSO were prepared of staurosporin, trametinib, and paclitaxel.

Seven days after adding the drugs, ATP levels were measured using the CellTiter-Glo 3-D Reagent (Promega, catalog no. G9681) according to the manufacturer's instructions, and luminescence was measured using a Spark multimode microplate reader (Tecan). Results were normalized to vehicle (100%) and baseline control (Staurosporin 1 μmol/L; 0%). For each line, when viability did not go above 70% or below 30%, an additional screen was performed for that particular drug with an adjusted dose of this drug for this organoid line. Screen quality was determined by checking *Z* factor scores for each plate following this formula:

$$Z = \frac{(3 \times SD(DMSO\ control)) + (3 \times SD(staurosporin\ control))}{(Average(DMSO\ control)) - (Average(staurosporin\ control))}.$$

The average *Z* factor score for all assays included in the manuscript was 0.7 (ranging from 0.40 to 0.81), which is consistent with an experimentally robust assay.

Whole-genome sequencing

Lab work

DNA was isolated from tumor tissue and organoid samples using the All Prep DNA/RNA Mini Kit (QIAGEN, Cat # 80204) following the manufacturer's instructions. For a blood germline reference, isolation of DNA from blood samples donated by corresponding patients was performed by USEQ (Utrecht Sequencing Facility) using the QIAGEN QIASymphony SP. Quality and quantification of DNA samples were checked with Qubit (DNA BR). DNA integrity and RNA contamination was assessed by using Tapestation DNA screens (Genomic screen) and Nanodrop (260/280 ratio). Per sample, 500–1,000 ng of DNA was used for DNA library preparation by USEQ using the TruSeq DNA Nano kit. Whole-genome sequencing was performed on NovaSeq 6000 to an average coverage of 30x for germline reference samples, and 60x to 90x for tumor tissue and organoid samples (see Table S4).

Early passage was defined as passages 1 to 3, intermediate passage as 4 to 6, and late passage as passages 7 and beyond.

Processing

Raw reads were processed using our in-house whole-genome sequencing processing workflow https://github.com/IARCbioinfo/alignment-nf v 1.2, which uses software bwa to align reads to reference genome GRCh38 with decoy genome and alt contigs, and GATK to perform base quality score recalibration. We performed quality controls using fastQC for raw reads and qualimap for aligned reads (using workflow https://github.com/IARCbioinfo/qualimap-nf v. 1.1), and confirmed that files of a same experiment came from the same individual using NGSCheckMate (using workflow https://github.com/IARCbioinfo/NGSCheckMate-nf v. 1.1a).

RNA sequencing

Lab work

We performed paired-end bulk RNA sequencing (RNA-seq) across 20 patients, including 1 patient with both primary tumor and metastasis, for a total of 18 parental tumor samples and 21 NEN PDTO lines that had been in culture for 6 to 67 weeks (Table S2). For 5 PDTO lines we captured expression patterns from 2 separate time points in culture. RNA was isolated as described above. RNA integrity was measured using the Agilent RNA 6000 Nano kit with the Agilent 2100 Bioanalyzer and RNA concentrations were determined using the Qubit RNA HS Assay Kit. RIN values of organoid RNA samples were typically 9–10 and only samples with RIN >8 were used for library preparation. RIN values of tissue RNA samples were typically 8–10, with 5 samples showing an RIN between 6.3 and 7.4, and only samples with RIN >6 were used for library preparation. RNA libraries were prepared using TruSeq Stranded mRNA polyA kit (Illumina) and sequenced on either an Illumina Nextseq 2000 (paired-end, 2 x 150 bp) or an Illumina Novaseq 6000 (paired-end, 2 x 150 bp). Library preparation and sequencing was performed by USEQ (Utrecht Sequencing Facility).

Processing

Processing of 47 RNA-seq from the experiments and public data for 210 RNA-seq from LNEN,[5] 30 LNETs,[6] and 88 RNA-seq from SINET[28,29] were all done using our RNA-seq pre-processing workflow (https://github.com/IARCbioinfo/RNAseq-nf v. 2.4) to ensure mitigation of potential batch effects between cohorts due to differences in processing (software, version, or operating system); as described in Gabriel et al.,[30] this workflow uses trimgalore to trim reads for adapter sequences and STAR to map reads to reference genome GRCh38. Base quality scores were then recalibrated to improve subsequent variant calling using GATK (https://github.com/IARCbioinfo/BQSR-nf v. 1.1), and alignments were realigned locally using ABRA2 to improve their quality, in particular at splicing junctions (https://github.com/IARCbioinfo/abra-nf v. 3.0).

Expression Quantification

Gene expression quantification was performed with Stringtie,[95] in one-pass mode, using our workflow https://github.com/IARCbioinfo/RNAseq-transcript-nf v 2.2 with the gencode v33 comprehensive gene annotation as reference, providing expression in raw read count and TPM formats. We also processed the SINET RNA-seq datasets EGA: EGAS00001003358 and SRA: SRP107025[28,29] with the same worflows, which is also the version that was used to process the LNEN data by Gabriel and colleagues,[30] allowing integration of the different datasets with minimal batch effects.

Unsupervised analyses

Analyses were performed separately on (i) lung and pancreatic NENs, and (ii) on small intestine NETs. Raw counts from all samples were normalized using the variance stabilization transform (R package DESeq2) to provide approximately normally distributed values, separately for (i) and (ii) and using the "blind" mode so each tumor type is processed in an independent and completely unsupervised manner (samples can have their own variance/mean relationship) but biologically meaningful differences between SINETs and other NENs are not removed. UMAP was then performed separately on (i) and (ii), using features known to be informative about molecular groups, and setting the number of neighbors to the maximal value (number of samples) so that both short- and long-distance relationships between samples are preserved, as in our recent integrative study.[30] The subset of genes for the lung and pancreatic NENs (i) were extracted from a published list of "core" genes that are differentially expressed between all pairs of lung NEN molecular groups,[5] excluding genes that were discarded between gencode v19 and v33 or that changed ENSEMBL ID between the releases (54/1459 genes). Cluster annotations were extracted from Gabriel et al.[30] (https://github.com/IARCbioinfo/DRMetrics/data/Attributes.txt.zip), assuming as shown in the article that clusters A1, A2, and B from Alcala et al.[5] respectively correspond to clusters LC1, LC3, and LC2 from Simbolo et al.,[8] and grouping together under the term LCNEC (resp. SCLC) LCNEC and LCNEC-like SCLC (resp. SCLC and SCLC-like LCNEC). The subset of genes for the SINET samples (ii) included all 520 genes from Alvarez et al.[28] except *NME1-NME2*, which is a readthrough transcription between neighboring genes *NME1* and *NME2* that was not quantified by StringTie.

Supervised analyses

A Partial Least Squares (PLS) analysis was performed on matched parental tumors ("parent" group) and PDTOs ("organoid" group) in order to find genes whose expressions are altered by the PDTO formation process, using the pls function from R package mixOmics in "regression" mode and selecting the first 10 components of the expression matrix (named *X* in the PLS framework, while the group matrix is *Y*), after running the variance stabilization transform on the entire dataset simultaneously using a design comparing the "parent" and "PDTO" groups, so differences between the groups is not removed during the transformation. PLS components separating parents and PDTOs were identified using ANOVA *F*-tests with each of the ten components as a function of the groups. We found only two components associated with the groups (F-tests, component 1, $p < 2.2\times10^{-16}$, component 2, $p = 0.01293$, other components $p > 0.35$).

To understand which genes were responsible for the separation between parents and PDTOs, we computed the Pearson correlation between the expression of each gene and each of the two PLS components associated with the groups and performed integrated gene set analysis on the correlation p values using the ActivePathways R package with GO terms as gene sets. ActivePathways allows combining p values from multiple sources (here components 1 and 2) to find which pathways are associated with each source separately and in combination. We found 108 significantly enriched pathways (see results in Figure S3G; Table S2). Pathways were then aggregated into super-pathways using the EnrichmentMap module of cytoscape, which forms a network of pathways based on their similarity in terms of shared genes, using the default cutoff of 0.375 similarity to connect two pathways. Results are presented Figure S3H, and show a vast majority (89/108) of pathways belonging to immune-related pathways and pathways sharing genes with these immune-related pathways. We also found two additional super pathways–one comprising four blood-vessel-related pathways and one comprising five synaptic-related pathways–a small group of 3 pathways and 6 additional isolated pathways.

Somatic alteration calling

Small variants calling

Single nucleotide variants were called from WGS data using software Mutect2 from GATK4 (using our workflow https://github.com/IARCbioinfo/mutect-nf v. 2.2b), and indels and multinucleotide variants were called using the intersection of Mutect2 and strelka2 calls (using our workflow https://github.com/IARCbioinfo/strelka2-nf v. 1.2a) in order to filter out false positive calls, more numerous in indels than in SNVs. Annotations were performed with ANNOVAR (using our workflow https://github.com/IARCbioinfo/table_annovar-nf v. 1.1.1). To ensure comparisons with previous studies on NETs[5,34] and common cancers,[96] that mostly relied on whole-exome sequencing, tumor mutational burdens were computed using the exonic ranges from the SureSelect Human All

Exon v7 panel from Agilent (bed file downloaded from the manufacturer's website, approximately covering 36Mb), and focusing on non silent mutations (nonsnononymous SNVs, nonsense mutations, nonstop mutations, and indels).

Small variants were called from RNA-seq data in the samples without WGS data using software Mutect2 from GATK4 as for WGS, but in tumor-only mode (also using our workflow https://github.com/IARCbioinfo/mutect-nf RNAseq branch) and annotated using ANNOVAR as described above. In addition, calls were further filtered using a random forest algorithm. See Alcala et al. (submitted) for a complete benchmarking of the algorithm using samples for which both RNA-seq and WGS was performed.[97] In summary, in the benchmarking, we show that around 40% of the driver mutations presented in Figures 4B and S4B were also present in the RNAseq (26/68), including at least one driver detected for all patients with at least one driver mutation detected from WGS. We used a machine learning approach to classify these 40% of variants detected in RNA-seq data as somatic or non-somatic (germline or sequencing artifact). We show that RNA-seq is sufficient to call somatic alterations with very good precision (up to 100%, see Figure 6 from Alcala et al. (submitted).[97] Because of the trade-off between sensitivity and specificity, we report variants with three levels of confidence. The high-sensitivity (73%) set, denoted by "*" in Figures 4C and S4C, has the interesting property of being likely to contain most somatic variants, but at the expense of being less specific (98%). The medium-sensitivity (62%) set, denoted by "**", is a compromise between sensitivity and specificity. Finally, the low-sensitivity (38%) set, denoted by "***", has the interesting property of likely only containing true somatic variants, but at the expense of missing a majority of actual somatic variants. Whenever a variant was found in either parental tumor or a PDTO, the corresponding position in the matched PDTO or parental tumor was classified as "no_coverage" whenever the read depth was 9 or less, below recommended depth for variant detection.[98]

Structural Variant Calling

Structural variants (SVs) were called from WGS data using a two-step ensemble method combining results from 3 software: SVaba,[99] Delly,[100] and Manta.[101] In the discovery step, following Mangiante et al.,[102] we independently called SVs in each of the 23 tumor samples with WGS data using the SURVIVOR consensus calling,[103] merging SVs within a distance of 1 kb and requiring either agreement between 2 SV callers or a strong support by a single caller (at least 15 reads), as implemented in our workflow (https://github.com/IARCbioinfo/sv_somatic_cns, v. 1.0). This step led to a list of high-quality SVs. In the subsequent recovery step, for each experiment and each SV that was not detected in all samples from this experiment, we checked whether one of the SV callers found reads supporting this SV with breakpoints within 1 kb of those detected (SVs marked as "recovered" in Table S4), in unfiltered calls from SVaba and Manta, and initial calls from DELLY (no unfiltered calls are reported by the software). SVs were annotated based on their type (inversion, translocation, duplication, deletion), the position of their breakpoints (intergenic, within exons or introns) and their strands as described in Mangiante et al. (2021), using the gencode v33 annotation.

Copy Number Variant calling

Copy number variants (CNVs) were called from WGS data using software PURPLE using our custom workflow https://github.com/IARCbioinfo/purple-nf (branch dev_multi-sample). This workflow relies on the recommended PURPLE workflow using AMBER for B-allele frequency (BAF) estimation and COBALT for read depth ratio (RDR) estimation (https://github.com/hartwigmedical/hmftools/tree/master/purple), but relying on multi-sample segmentation of using the multipcf function from R package copynumber[104] instead of the simple pcf function used in the recommended workflow; this allows to infer more consistent breakpoints across samples from the same experiment. In addition, we used the option to include the list of SNVs called by Mutect2 (see above) to improve the CNV estimation by using the variant allelic fractions.

Analyses

We identified as damaging mutations the nonsynonymous mutations predicted as damaging by REVEL (score greater than or equal to 0.5) which combines multiple other damage predictions to maximize the evidence of pathogenicity,[105] along with stop gains, stop losses, indels, and splicing mutations. We retrieved driver gene lists from a literature search of lung and SI neuroendocrine neoplasms[7,34,36,38–41,106–109] (see Table S4 for the complete list). The waterfall plots (Figures 4B and 4C) were produced using R package maftools.[110] Circos plots were produced using R package circlize.[111]

Mutational signatures

Small variants

Signatures were extracted from the VCFs using SigProfilerExtractor, comparing decompositions with 2–10 *de novo* signatures and using the number of signatures maximizing stability while minimizing cosine differences in signature reconstruction. Temporal signature activities were reconstructed using R package TrackSig separately on public (present in both parent and PDTO) and private alterations (present only in one sample). All signatures are reported in Figure S5 and Table S4, and signatures known to be due to sequencing artifacts were removed and signature contributions normalized to sum to 100% for Figure 5.

Evolutionary analyses

Mutation clustering and clonality

Somatic alterations were clustered and classified as clonal or subclonal using deconvolution of VAF distributions with R package DPclust.[112] Input files were prepared using R package dpclust3p, focusing on alterations with good coverage (above the target depth, 30X or 60X depending on the samples; see Table S4) and in clonal CNVs regions with consistent CN estimates in at least 2 samples from the same line for more accurate reconstructions. We used 5000 iterations after a burn-in phase of 1000 iterations. DPclust computed cancer cell fractions (CCFs) based on VAF and CN states and provided a likelihood that each alteration belongs to each cluster. In order to obtain high-confidence clonal reconstruction, we assigned alterations to a given cluster only if their

likelihood to belong to this cluster was greater than or equal to 95%; other alterations were classified as "Uncertain" clustering. Clusters with less than 2.5% of assigned alterations were excluded. Clusters with an estimated location above a CCF of 0.95 in all samples were considered clonal. We summed up the likelihoods of belonging to each subclonal cluster, and considered alterations with a likelihood sum greater than or equal to 95% as subclonal. Venn-euler diagrams of shared clonal and subclonal alterations in Figure 5A were computed using R package eulerr.

Clonality of driver small variant alterations not included in the DPclust model fit was subsequently assessed by finding the closest cluster in terms of CCF considering only alterations with the same CN as the focal driver variant. Clonality of CNVs was assessed using PURPLE estimated allelic fractions, with CNVs with both minor and major allele copy number estimates close to an integer value (with a threshold of 0.2) considered clonal, and the rest as subclonal. Clonality of structural variants was assessed by averaging the variant allelic fraction reported by each of the three callers and comparing with the expected clonal allelic fraction given the tumor purity. Clonality of the chromothripsis event in LNET10 was assessed using the clonality of the involved CNV segments (in particular in chr1 and chr9) and the allelic fractions of structural variants estimated from the proportion of supporting reads in the structural variants clustered in the involved regions (chr1, chr4, chr9, and chr16).

Phylogenies and fishplots

We used clonevol[113] to reconstruct tumor phylogenies between clusters. In order to account for the uncertainty in estimating the centroid of mutation clusters from CCF distributions, for each cluster we randomly sampled centroid positions from normal distributions centered on the estimated value and with a standard deviation equal to the observed standard deviation of CCF values for this cluster. We then ran clonevol independently on each randomly sampled centroid, and selected 20 resulting possible phylogenies; we selected the replicate with the CCF centroids closest to the point estimate for visualization. We plotted the results using R package fishplot.[114] Because no clonal cluster and alterations were identified for LNET2, we used a polyclonal model; for all other samples, a clonal cluster was found and we used a monoclonal model. Note that alterations absent from a sample but that cluster with alterations at a non-zero frequency in this sample are thus inferred as part of a subclone detected in the focal sample; such mutations usually have a lower coverage in the focal sample, explaining the detection failure. In particular, although absent from sample LCNEC4 organoids, the *APC* and *PTPRZ1* mutations reported in Figure 4B were detected at a very low allelic fraction (6 and 7%, respectively) and were assigned to cluster 2 from Figure S5A, which is at low but non-zero frequency in the PDTOs (Figure 5B), and indeed coverage at their positions in the PDTOs were lower than in the original tumor (59 and 24 vs. 89 for *APC*, and 96 and 24 vs. 109 for *PTPRZ1*), making failure of detecting them if present in this cluster likely. Similarly, the *ERCC6L* mutation in LNET2 and the *SMARCA4*, *ATR*, and *NTRK3* mutations were all assigned to low frequencies clones even though undetected in the corresponding sample.

Diversity summary statistics

Levels of intra-tumor genetic diversity were computed using the effective number of alleles Δ,[115] a measure widely used in ecology and conservation genetics to monitor the level of genetic diversity in species of conservation interest.[116] In the case of biallelic markers such as somatic small variants, Δ is a genetic diversity metric which ranges from 1 (no diversity) to 2 (maximal diversity) and captures how many alleles are effectively segregating in the population at a given polymorphic site; for example, given a polymorphic site with two alleles, A at a high frequency 0.999 and B at a low frequency 0.001, although two alleles are present, because allele B is only present in a fraction of individuals, the *effective* number of alleles is $1.002 \simeq 1$. In order to obtain a quantity analogous to the tumor mutational burden, we rather focus on Δ-1, the effective number of *alternative* alleles (i.e., not taking into account the reference allele), and compute its sum across all polymorphic sites:

$$\Delta_T = \sum_i (\Delta_i - 1),$$

where $\Delta_i = 1/(CCF_i^2 + (1\text{-}CCF_i)^2)$ and CCF_i is the cancer cell fraction of the alternative allele at site i. We name this metric "effective number of alterations", and further divide it by the size of the genomic ranges (in Mb) from which the alternative alleles were called. The resulting quantity ranges from 0, when there are no subclonal alterations or when all subclonal alterations have infinitesimal values, to the subclonal TMB when all clonal alterations are present in exactly half of the tumor cells (CCF = 0.5, the situation maximizing diversity). All diversity statistics were computed using Nei and Chesser's estimators.[117]

Mode of evolution

Neutral evolution was detected from the distribution of subclonal alterations using R package MOBSTER.[44] MOBSTER uses a mixture model to identify a "neutral tail" in the distribution of CCF indicating the presence of a neutrally evolving subclone. For each sample, we filtered out alterations with a CCF below 5% and independently fitted models with and without neutral tails and with up to 4 additional subclones, and chose the best model using the reduced reduced Integrated Classification Likelihood (relCL) statistic.

QUANTIFICATION AND STATISTICAL ANALYSES

Temporal trends in passage times were tested using Mann-Kendall trend tests as implemented in the R package trend, for each sample individually. Resulting p values were adjusted for multiple testing using the Benjamini-Hochberg procedure.[118]

Cancer Cell, Volume *41*

Supplemental information

Druggable growth dependencies and tumor evolution analysis in patient-derived organoids of neuroendocrine neoplasms from multiple body sites

Talya L. Dayton, Nicolas Alcala, Laura Moonen, Lisanne den Hartigh, Veerle Geurts, Lise Mangiante, Lisa Lap, Antonella F.M. Dost, Joep Beumer, Sonja Levy, Rachel S. van Leeuwaarde, Wenzel M. Hackeng, Kris Samsom, Catherine Voegele, Alexandra Sexton-Oates, Harry Begthel, Jeroen Korving, Lisa Hillen, Lodewijk A.A. Brosens, Sylvie Lantuejoul, Sridevi Jaksani, Niels F.M. Kok, Koen J. Hartemink, Houke M. Klomp, Inne H.M. Borel Rinkes, Anne-Marie Dingemans, Gerlof D. Valk, Menno R. Vriens, Wieneke Buikhuisen, José van den Berg, Margot Tesselaar, Jules Derks, Ernst Jan Speel, Matthieu Foll, Lynnette Fernández-Cuesta, and Hans Clevers

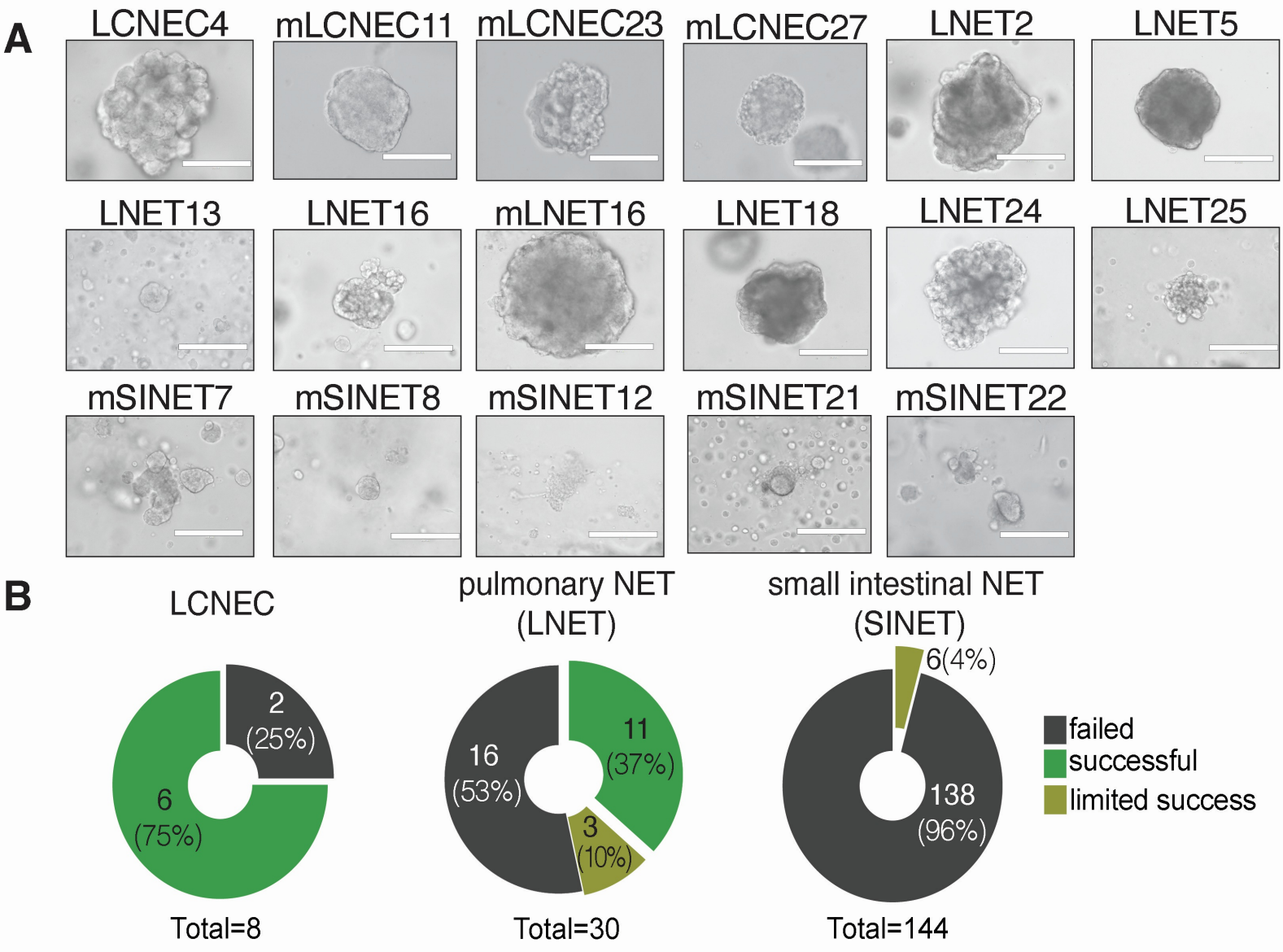
A
LCNEC4
mLCNEC11
mLCNEC23
mLCNEC27
LNET2
LNET5
LNET13
LNET16
mLNET16
LNET18
LNET24
LNET25
mSINET7
mSINET8
mSINET12
mSINET21
mSINET22
B
LCNEC
pulmonary NET (LNET)
small intestinal NET (SINET)
2 (25%)
6 (75%)
16 (53%)
11 (37%)
3 (10%)
6(4%)
138 (96%)
failed
successful
limited success
Total=8
Total=30
Total=144

Figure S1. Establishment of a NEN PDTO biobank, related to Figure 1.

(A) Representative bright-field images of PDTOs. Scale bar: 200 μm except for mSINET12 where scale bar is 400 μm.

(B) Success rate to establish PDTOs from isolated LCNEC, lung NET (LNET), and small intestinal NET (SINET) tissue. Limited success indicates lines for which molecular data was generated but that subsequently stopped growing. Not shown: tissue from pancreatic NETs was also collected for this study but organoid generation was unsuccessful in all cases.

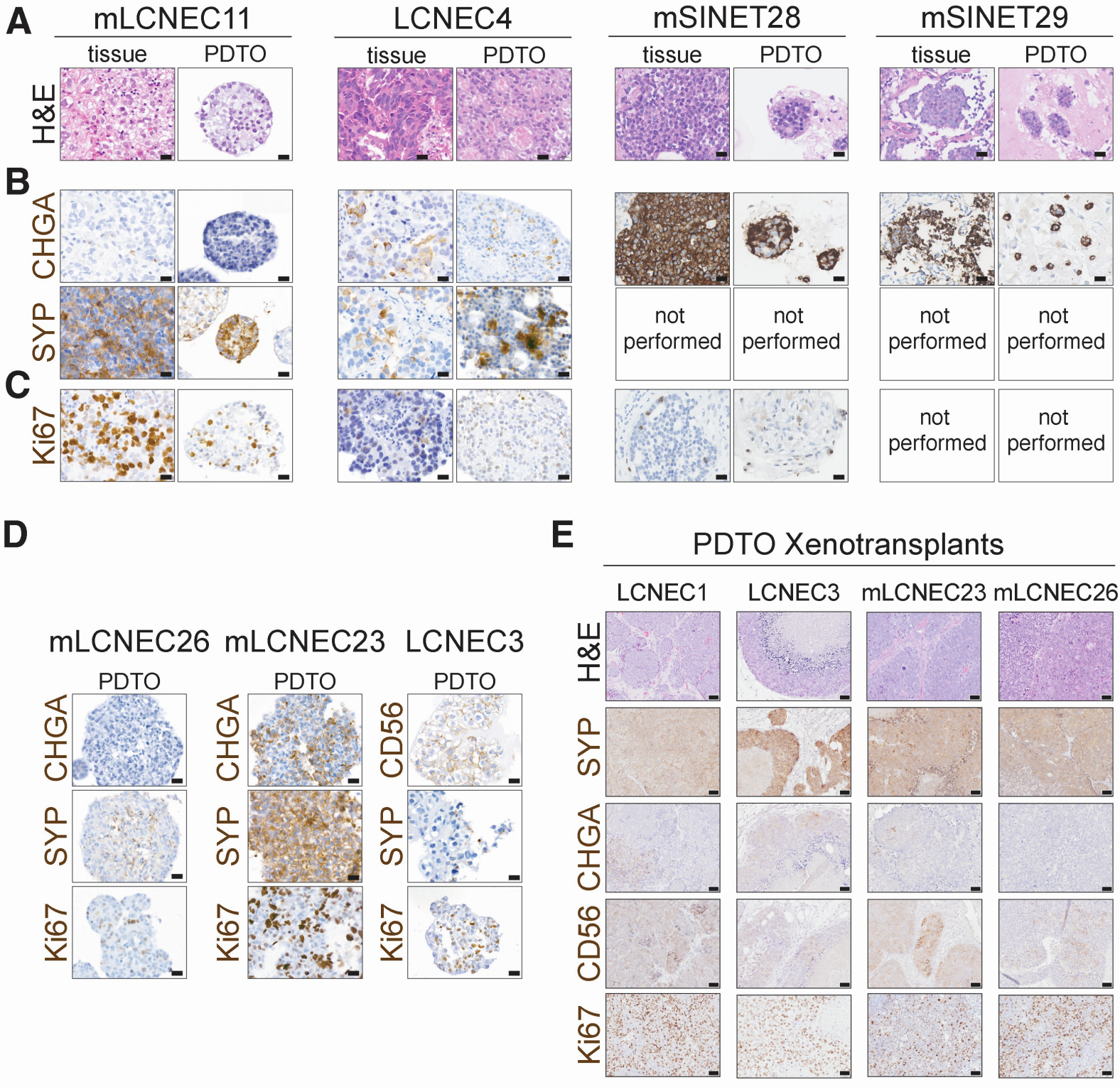
A
mLCNEC11
LCNEC4
mSINET28
mSINET29
tissue
PDTO
H&E
B
CHGA
SYP
C
Ki67
not performed
D
mLCNEC26
mLCNEC23
LCNEC3
CD56
E
PDTO Xenotransplants
LCNEC1

Figure S2. NET and LCNEC PDTOs retain histologic features of parental tumor subtypes, related to Figure 2

(A-C) Representative images of (A) hematoxylin and eosin (H&E) and immunohistochemical staining for (B) the neuroendocrine marker, Chromogranin A (CHGA) and (C) the proliferation marker Ki67 of PDTOs and their corresponding parental tumor tissue. Scale bar: 20 μm. mSINET: metastasis of small intestine NET; mLCNEC: metastasis of LCNEC.

(D) Representative images of immunohistochemical staining for the neuroendocrine markers, Chromogranin A (CHGA) or CD56, and Synaptophysin (SYP), and the proliferation marker Ki67 of LCNEC PDTOs for which parental tissue was not available.

(E) Representative images of H&E staining and immunohistochemical staining for the neuroendocrine markers, CHGA, SYP, and CD56, and the proliferation marker Ki67 of LCNEC PDTO-Xenotransplants. Scale bar: 50 μm.

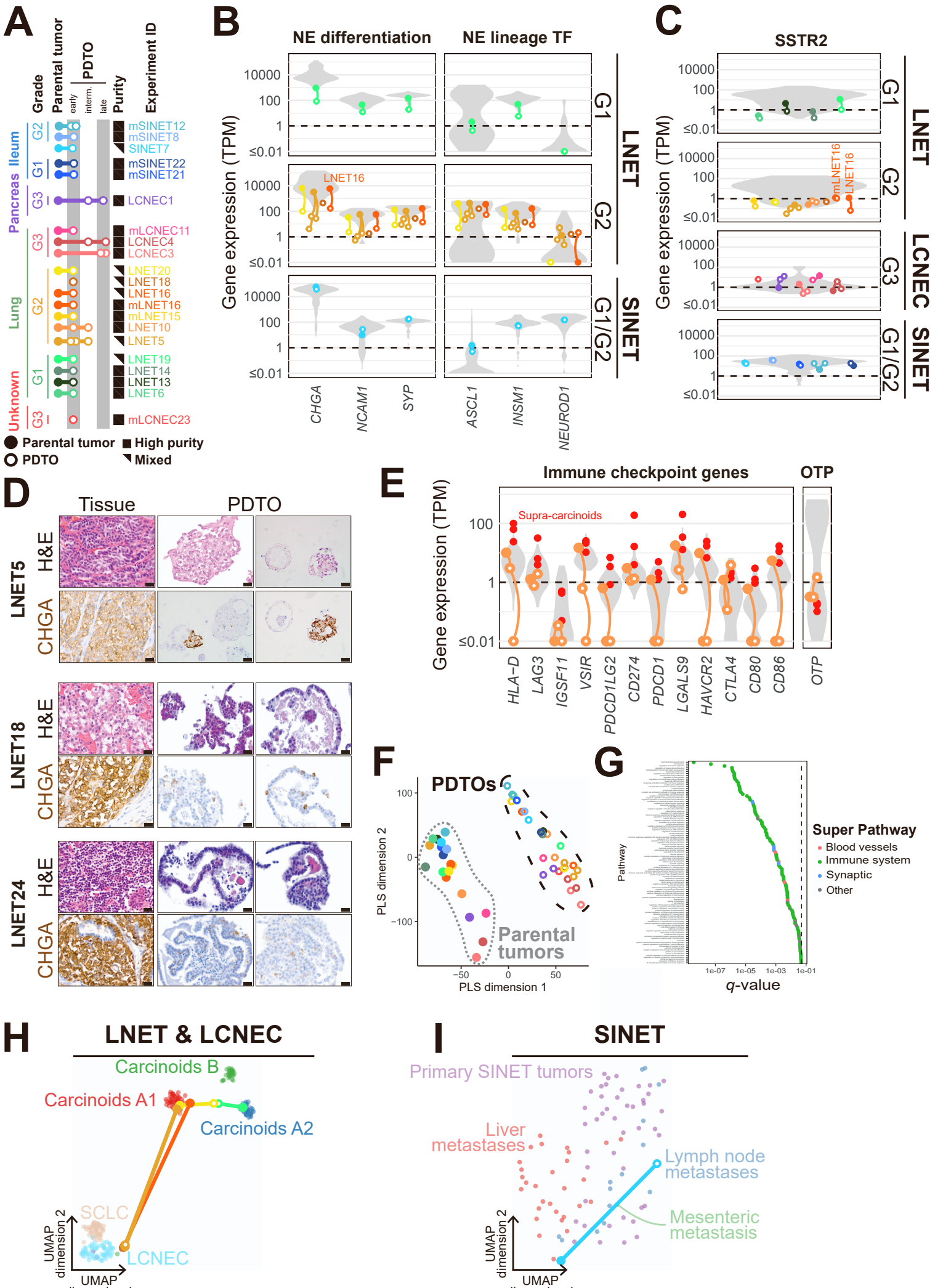
A
Grade
Parental tumor
PDTO
early
interm.
late
Purity
Experiment ID
Pancreas
Ileum
Lung
Unknown
G2
G1
G3
mSINET12
mSINET8
SINET7
mSINET22
mSINET21
LCNEC1
mLCNEC11
LCNEC4
LCNEC3
LNET20
LNET18
LNET16
mLNET16
mLNET15
LNET10
LNET5
LNET19
LNET14
LNET13
LNET6
mLCNEC23
Parental tumor
PDTO
High purity
Mixed
B
NE differentiation
NE lineage TF
Gene expression (TPM)
10000
100
1
≤0.01
LNET16
G1
G2
G1/G2
LNET
SINET
CHGA
NCAM1
SYP
ASCL1
INSM1
NEUROD1
C
SSTR2
mLNET16
LNET16
LCNEC
D
Tissue
PDTO
LNET5
LNET18
LNET24
H&E
CHGA
E
Immune checkpoint genes
OTP
Supra-carcinoids
100
1
≤0.01
HLA-D
LAG3
IGSF11
VSIR
PDCD1LG2
CD274
PDCD1
LGALS9
HAVCR2
CTLA4
CD80
CD86
OTP
F
PDTOs
Parental tumors
PLS dimension 2
PLS dimension 1
100
0
−100
−50
0
50
G
Pathway
Super Pathway
Blood vessels
Immune system
Synaptic
Other
1e-07
1e-05
1e-03
1e-01
q-value
H
LNET & LCNEC
Carcinoids B
Carcinoids A1
Carcinoids A2
SCLC
LCNEC
UMAP dimension 2
UMAP dimension 1
I
SINET
Primary SINET tumors
Liver metastases
Lymph node metastases
Mesenteric metastasis
UMAP dimension 2
UMAP dimension 1

Figure S3. Expression analyses, related to Figure 3.

(A) Extended panel 3A: outline of samples submitted to RNAseq

(B) mRNA expression of neuroendocrine markers in mixed PDTOs and parental tumors. Gray violin plots represent reference profiles with matching histological type and grade (*n*=75 for G1 LNET, *n*=40 for G2 LNET, *n*=69 for LCNEC, *n*=88 for SINET).

(C) SSTR2 mRNA expression in all samples. Gray violin plots represent reference profiles with matching histological type and grade (*n*=75 for G1 LNET, *n*=40 for G2 LNET, *n*=69 for LCNEC, *n*=88 for SINET).

(D) Immunohistochemical staining for CHGA in low purity PDTOs. Scale bar: 20 µm

(E) mRNA expression of immune checkpoint genes and *OTP* in LNET10. Gray violin plots represent reference profiles with matching histological type and grade (*n*=40 G2 LNET), including three supra-carcinoids (red points).

(F) Partial Least Squares (PLS) of PDTOs and tumors.

(G) Gene set enrichment analysis of PLS components separating parental tumors and PDTOs.

(H) UMAP of mixed LNET & LCNEC PDTOs.

(I) UMAP of the mixed SINET PDTO.

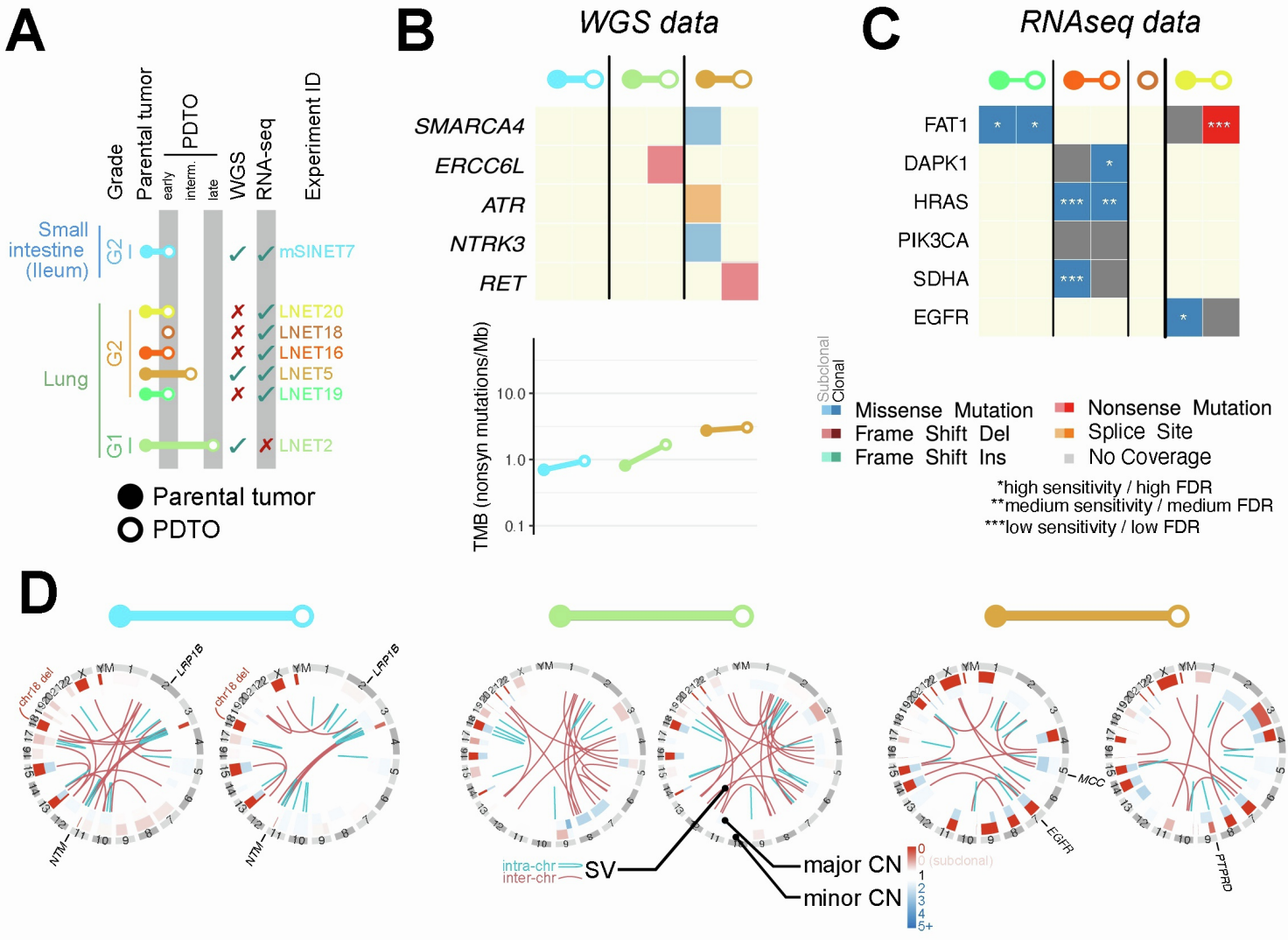
A
Grade
Parental tumor
PDTO
early
interm.
late
WGS
RNA-seq
Experiment ID
Small intestine (Ileum)
G2
mSINET7
Lung
G2
LNET20
LNET18
LNET16
LNET5
LNET19
G1
LNET2
Parental tumor
PDTO
B
WGS data
SMARCA4
ERCC6L
ATR
NTRK3
RET
TMB (nonsyn mutations/Mb)
10.0
1.0
0.1
C
RNAseq data
FAT1
DAPK1
HRAS
PIK3CA
SDHA
EGFR
Subclonal
Clonal
Missense Mutation
Frame Shift Del
Frame Shift Ins
Nonsense Mutation
Splice Site
No Coverage
*high sensitivity / high FDR
**medium sensitivity / medium FDR
***low sensitivity / low FDR
D
chr18 del
LRP1B
NTM
MCC
EGFR
PTPRD
intra-chr
inter-chr
SV
major CN
minor CN
0
0 (subclonal)
1
2
3
4
5+

Figure S4. Genomic profiles of mixed PDTOs, related to Figure 4.

(A-D) All panels correspond to those in **Figure 4**, but focus on mixed-purity PDTOs. (A) Overview of mixed-purity PDTOs and parental tumors for which whole genome sequencing (WGS) and/or RNA-seq data was generated. Filled circles: parental tumors; empty circles: PDTOs (early passage: 1-3; intermediate passage: 4-7; late passage: 8+).

(B-C) Summary of putative pathogenic somatic alterations detected by (B) WGS or (C) RNA-seq in genes reported to be recurrently mutated in LCNEC, LNET, and SINET. Colors represent variant classes and clonality (light: subclonal; solid: clonal). In (B), the lower panel represents the Tumor Mutational Burden (TMB); the number of nonsynonymous mutations per megabase. In (C), light gray represents genes without enough coverage to detect variants. The *EGFR* mutation in LNET20 is a non-recurrent mutation (T227C, COSMIC ID COSV51767338) reported once in an acute lymphoblastic T cell leukemia tumor (PMID: 22675565); (D) Structural variants in PDTOs and parental tumors. Inner layer: chromosomal rearrangements; central layer: major copy number (CN); outer layer: minor CN. Structural variants damaging genes that have been previously reported as recurrently mutated in LCNEC, LNET, or SINET are annotated in black. Subclonal CN alterations (non-integer CN) are indicated with intermediate colors (e.g., light red for subclonal CN loss). The EGFR SV in LNET5 is an inversion of the 54,719,987–55,202,337 region (starting before exon 1 and ending in the intronic region between exons 26 and 27, out of the 28 exons of the main transcript ENST00000275493.7), with limited spanning and split reads support (13/126 and 8/123, respectively) suggesting a low-frequency subclonal alteration.

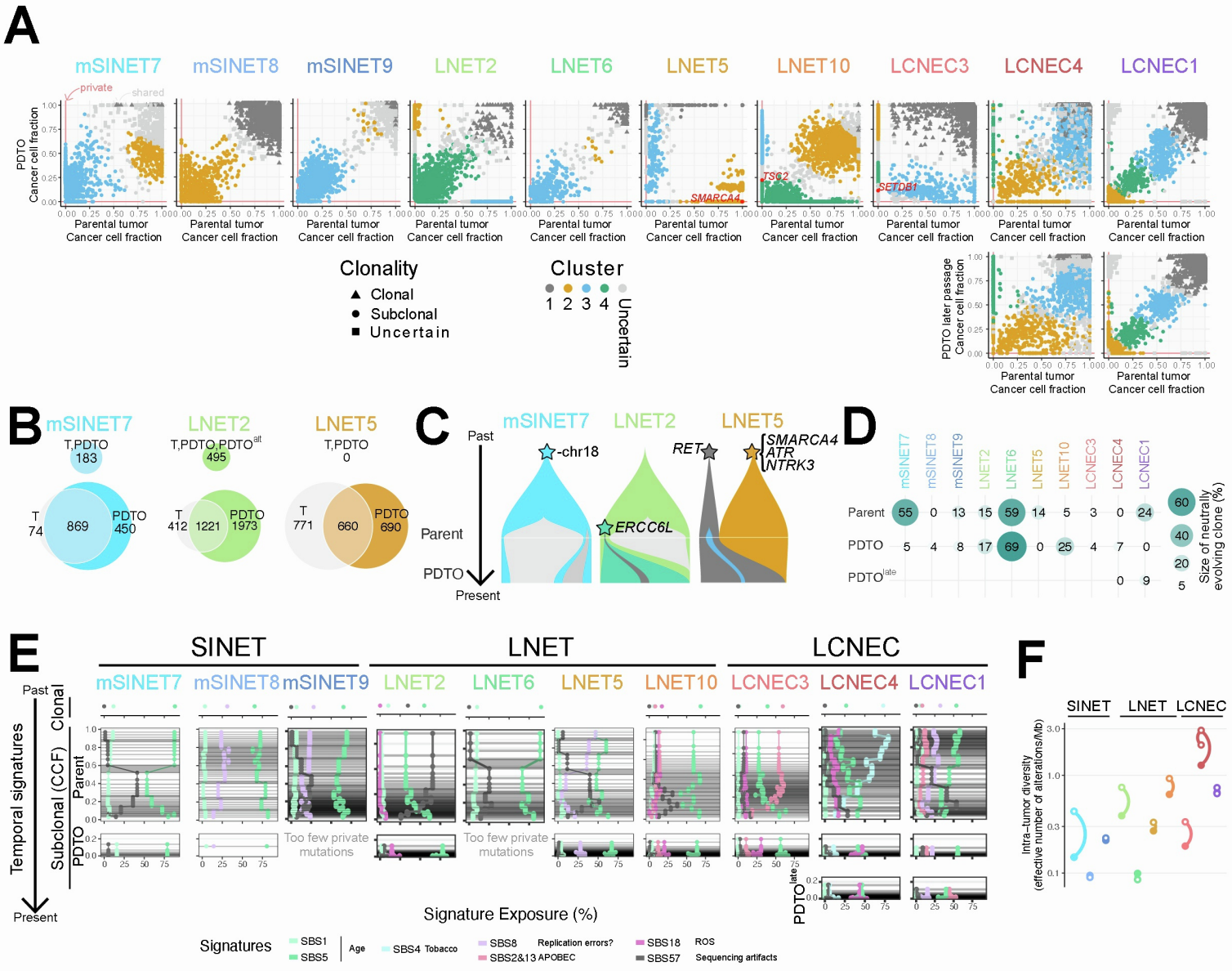
A
mSINET7
mSINET8
mSINET9
LNET2
LNET6
LNET5
LNET10
LCNEC3
LCNEC4
LCNEC1
private
shared
PDTO Cancer cell fraction
Parental tumor Cancer cell fraction
SMARCA4
TSC2
SETDB1
Clonality
Clonal
Subclonal
Uncertain
Cluster
1 2 3 4 Uncertain
PDTO later passage Cancer cell fraction
B
mSINET7
T,PDTO 183
T 74
869
PDTO 450
LNET2
T,PDTO,PDTO^alt 495
T 412
1221
PDTO 1973
LNET5
T,PDTO 0
T 771
660
PDTO 690
C
Past
Parent
PDTO
Present
mSINET7
-chr18
LNET2
ERCC6L
LNET5
RET
SMARCA4
ATR
NTRK3
D
mSINET7
mSINET8
mSINET9
LNET2
LNET6
LNET5
LNET10
LCNEC3
LCNEC4
LCNEC1
Parent 55 0 13 15 59 14 5 3 0 24
PDTO 5 4 8 17 69 0 25 4 7 0
PDTO^late 0 9
Size of neutrally evolving clone (%)
60
40
20
5
E
SINET
LNET
LCNEC
mSINET7
mSINET8
mSINET9
LNET2
LNET6
LNET5
LNET10
LCNEC3
LCNEC4
LCNEC1
Past
Present
Temporal signatures
Clonal
Subclonal (CCF)
Parent
PDTO
Too few private mutations
Too few private mutations
PDTO^late
Signature Exposure (%)
Signatures
SBS1
SBS5
Age
SBS4 Tobacco
SBS8
SBS2&13 APOBEC
Replication errors?
SBS18
SBS57
ROS
Sequencing artifacts
F
SINET
LNET
LCNEC
Intra-tumor diversity (effective number of alterations/Mb)

Figure S5. Extended Figure 5 including mixed PDTOs, related to Figure 5.
(A) Clustering of joint cancer cell fractions (CCF) of small variants in regions with clonal copy number alterations. Colors correspond to clusters, and shapes to clonality.
(B) Venn-Euler diagrams of shared and private clonal (top) and subclonal (bottom) somatic small variants from mixed samples.
(C) Fish plots showing clonal reconstruction of tumor and organoid from mixed samples.
(D) Mode of evolution, measured as the size of the neutrally evolving clone in percentage of subclonal alterations (see methods), for both high-purity and mixed-purity samples.
(E) Extended Figure 5(D), including both high-purity and mixed-purity samples, and proportions of alterations from artifactual mutational signature SBS57. Temporal mutational signatures, measured as the signature exposure (the percentage of mutations belonging to each signature), in clonal small variants (top), subclonal small variants present only in the parental tumor (middle), and those only present in the PDTO (bottom). The vertical axis corresponds to the cancer cell fraction (CCF), a proxy for the age of the mutation (older alterations: top; high CCF, recent alterations: bottom; low CCF).
(F) Extended Figure 5(E): Intra-tumor genetic diversity, the effective number of alterations per Mb (see methods) in both high-purity and mixed-purity samples.

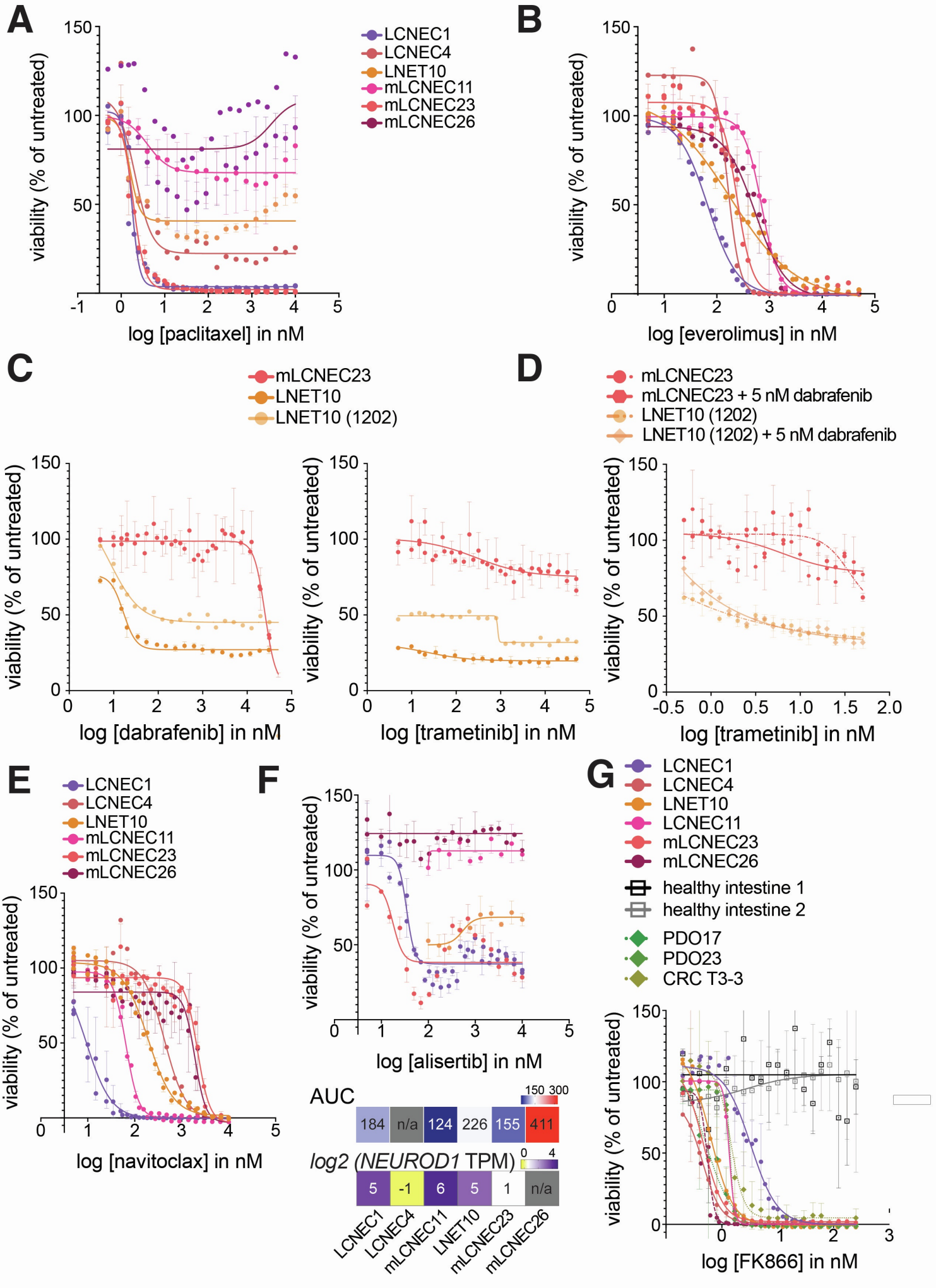
A
viability (% of untreated)
log [paclitaxel] in nM
LCNEC1
LCNEC4
LNET10
mLCNEC11
mLCNEC23
mLCNEC26
B
viability (% of untreated)
log [everolimus] in nM
C
mLCNEC23
LNET10
LNET10 (1202)
viability (% of untreated)
log [dabrafenib] in nM
viability (% of untreated)
log [trametinib] in nM
D
mLCNEC23
mLCNEC23 + 5 nM dabrafenib
LNET10 (1202)
LNET10 (1202) + 5 nM dabrafenib
viability (% of untreated)
log [trametinib] in nM
E
LCNEC1
LCNEC4
LNET10
mLCNEC11
mLCNEC23
mLCNEC26
viability (% of untreated)
log [navitoclax] in nM
F
viability (% of untreated)
log [alisertib] in nM
AUC
150 300
184 n/a 124 226 155 411
log2 (NEUROD1 TPM)
0 4
5 -1 6 5 1 n/a
LCNEC1
LCNEC4
mLCNEC11
LNET10
mLCNEC23
mLCNEC26
G
LCNEC1
LCNEC4
LNET10
LCNEC11
mLCNEC23
mLCNEC26
healthy intestine 1
healthy intestine 2
PDO17
PDO23
CRC T3-3
viability (% of untreated)
log [FK866] in nM

Figure S6. Dose-response curves, related to Figure 6

(A-B) Dose-response curves for (A) Paclitaxel or (B) Navitoclax. Dots and error bars represent the mean and SEM from assays repeated on different days, respectively (*n* = 3-4), except for LCNEC4 where they represent technical replicates from one assay.
(C) Dose-response curves for Dabrafenib or Trametinib. Dots and error bars represent the mean and SEM from assays repeated on different days (*n* = 3), respectively. Shown also are the values from an assay on LNET10, (LNET10 (1202)), which correspond to one technical replicate that deviated from the others.
(D) Dose-response curves for treatments with Trametinib alone or in combination with 5 nM Dabrafenib. Dots and error bars represent the mean and SEM from technical replicates (*n* = 3), respectively.
(E) Dose-response curves for Navitoclax. Dots and error bars represent the mean and SEM from assays repeated on different days, respectively (*n* = 3-4), except for LCNEC4 where they represent technical replicates from one assay.
(F) Dose-response curves for Alisertib. Dots and error bars represent the mean and SEM from technical replicates (*n* = 3), respectively. Bottom panels show expression values for *NEUROD1*, and the AUC calculated for all samples tested.
(G) Dose-response curves for FK866. Dots and error bars represent the mean and SEM from assays repeated on different days, respectively (*n* = 2-4), except for LCNEC4 and mLCNEC11 where they represent technical replicates from one assay. PDO17 and PDO23, 2 pancreatic ductal adenocarcinoma PDTOs; CRC, colorectal cancer PDTOs (1 line).

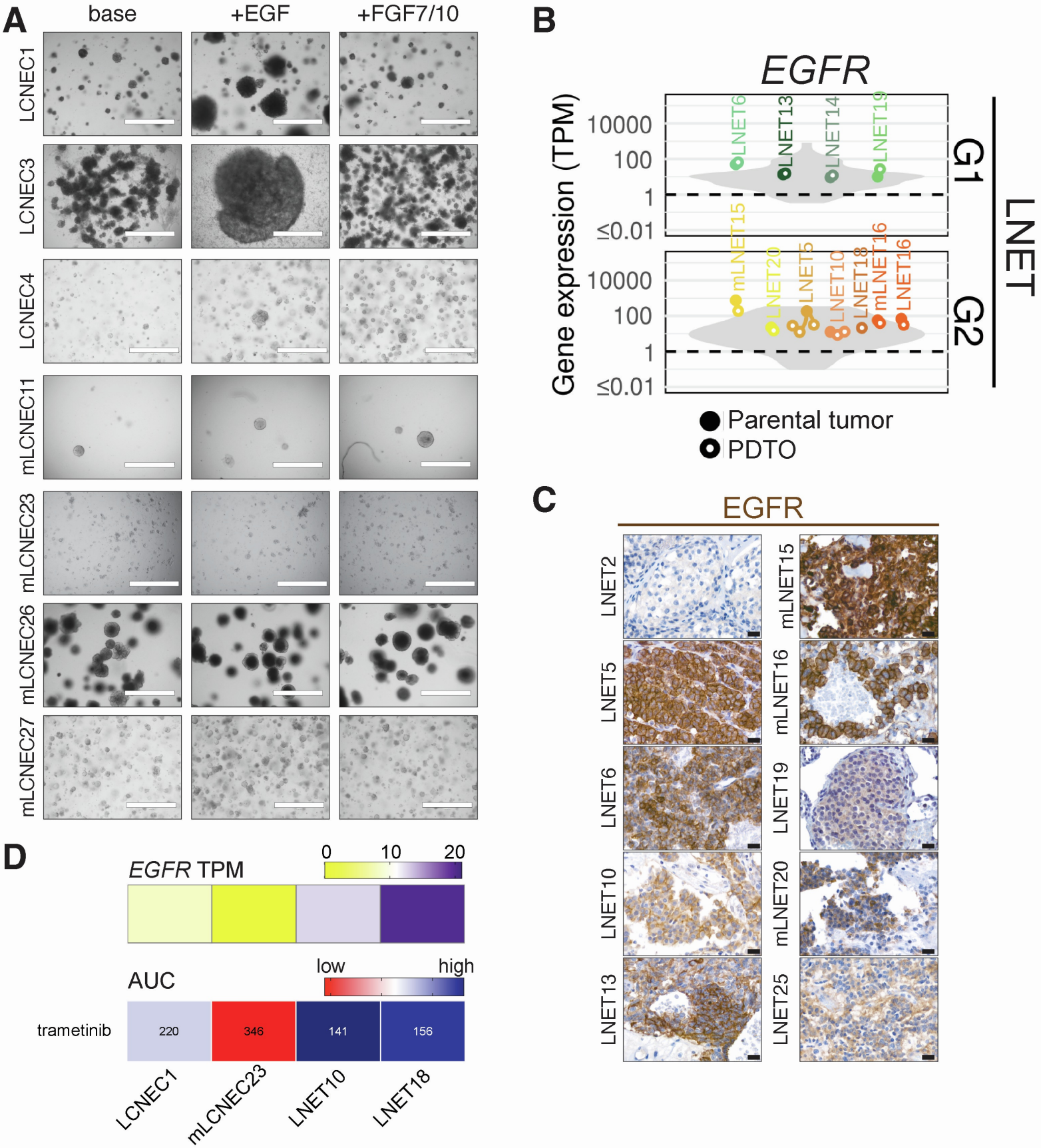
A
base
+EGF
+FGF7/10
LCNEC1
LCNEC3
LCNEC4
mLCNEC11
mLCNEC23
mLCNEC26
mLCNEC27
B
EGFR
Gene expression (TPM)
10000
100
1
≤0.01
LNET6
LNET13
LNET14
LNET19
mLNET15
LNET20
LNET5
LNET10
LNET18
mLNET16
LNET16
G1
G2
LNET
Parental tumor
PDTO
C
EGFR
LNET2
LNET5
LNET6
LNET10
LNET13
mLNET15
mLNET16
LNET19
mLNET20
LNET25
D
EGFR TPM
0
10
20
AUC
low
high
trametinib
220
346
141
156
LCNEC1
mLCNEC23
LNET10
LNET18

Figure S7. EGFR dependency, related to Figure 7

(A) Brightfield images showing LCNEC PDTO outgrowth in base NEN media and media supplemented with EGF or with FGF7 and FGF10. Scale bar: 1000 μm

(B) Expression of *EGFR* parental tumors and matched PDTOs, in units of transcripts per million (TPM), for pulmonary NETs of different grades. Gray violin plots represent reference profiles with matching histological type and grade (*n*=75 for G1 LNET, *n*=40 for G2 LNET)

(C) Immunohistochemical staining for the EGF receptor, EGFR, in parental tumor tissue for PDTO lines reported in this manuscript. Scale bar: 20 μm

(D) Heat-map showing sensitivity of LNET18, LNET10, and LCNEC PDTO lines to the MEK inhibitor, trametinib, as measured by area under the curve (AUC). Numerical values for AUC are shown. Red indicates high AUC values, blue indicates low AUC values. AUC is reported instead of IC50 values, because the dose response curve did not allow for IC50 value calculation. Expression of *EGFR* for each PDTO line tested are also shown (in TPM).